2016

Extrinsic Effects on Heat and Electron Transport In Two-Dimensional Van-Der Waals Materials- A Boltzmann Transport Study

Arnab K. Majee
University of Massachusetts Amherst

EXTRINSIC EFFECTS ON HEAT AND ELECTRON TRANSPORT IN TWO-DIMENSIONAL VAN-DER WAALS MATERIALS —A BOLTZMANN TRANSPORT STUDY

A Thesis Presented

by

ARNAB KUMAR MAJEE

Submitted to the Graduate School of the
University of Massachusetts Amherst in partial fulfillment
of the requirements for the degree of

MASTER OF SCIENCE IN ELECTRICAL AND COMPUTER ENGINEERING

September 2016

Electrical and Computer Engineering

EXTRINSIC EFFECTS ON HEAT AND ELECTRON TRANSPORT IN TWO-DIMENSIONAL VAN-DER WAALS MATERIALS —A BOLTZMANN TRANSPORT STUDY

A Thesis Presented

by

ARNAB KUMAR MAJEE

Approved as to style and content by:

Zlatan Aksamija, Chair

Neal Anderson, Member

Eric Polizzi, Member

Christopher V. Hollot, Department Chair
Electrical and Computer Engineering

DEDICATION

To my family members

ACKNOWLEDGMENTS

I would, forever, be grateful to my advisor, Professor Zlatan Aksamija, for his thoughtful, patient guidance and support. Special thanks to Professor Eric Polizzi and Professor Neal Anderson, for kindly serving as my thesis committee and providing valuable inputs that improved the quality of this study. I, sincerely, thank Cameron J. Foss for calculating the electronic bandstructures for graphene and MoS_2.

I am also thankful to my parents and friends for their constant support and motivation.

ABSTRACT

EXTRINSIC EFFECTS ON HEAT AND ELECTRON TRANSPORT IN TWO-DIMENSIONAL VAN-DER WAALS MATERIALS —A BOLTZMANN TRANSPORT STUDY

SEPTEMBER 2016

ARNAB KUMAR MAJEE

B.Tech., WEST BENGAL UNIVERSITY OF TECHNOLOGY

M.S.E.C.E., UNIVERSITY OF MASSACHUSETTS AMHERST

Directed by: Professor Zlatan Aksamija

Two-dimensional van der Waals materials have been a subject of intense research interest in recent years. High thermal conductivity of graphene can be utilized for many thermal management applications. In spite of possessing very high electron mobility, graphene can't be used as transistors because of the absence of band gap; however transition metal dichalcogenides are another class of two-dimensional van der Waals materials with inherent band gap and show a great promise for future nanoelectronic applications. But in order to tailor these properties for commercial applications, we should develop a better understanding of the effect of extrinsic factors like size, rough edges, grain boundaries, mass-impurities, interaction with substrate etc. on thermal and electrical transport.

Most materials exhibit a smooth ballistic-to-diffusive type of thermal transport in which when the sample size is small as compared to mean-free-path of phonons the transport is ballistic, whereas, when the sample size is large as compared to phonon mean-free-path, phonons undergo multiple scattering events and the thermal transport becomes diffusive in

nature. However, graphene exhibits an atypical thermal transport behavior where thermal conductivity shows an increasing logarithmic trend even for samples far greater than the mean-free-path of phonons. We show that this anomalous behavior can be attributed to the significant contribution coming from momentum-conserving normal phonon-phonon scattering. Secondly, graphene grain boundaries have been found to significantly reduce thermal conductivity even in the presence of substrates. In spite of numerous studies on the effect of grain boundaries (GBs) on thermal conductivity in graphene, there lacks a complete correlation between GB resistance and misorientation angle across graphene GBs. We show a direct correlation between thermal GB resistance and mismatch angles with low angle mismatch can be captured only by GB roughness, whereas, large mismatch angles will lead to the formation of a disordered patch at the interface and it could significantly deteriorate the overall thermal conductivity even in the presence of substrates.

GBs are found to affect electrical transport in two-dimensional systems as well. Owing to the excellent electronic properties and compactness of these two-dimensional materials, high quality 2D heterojunctions are the subject of intense research interest in recent years. Graphene-MoS_2 heterojuctions are found to form ohmic contacts and show great potential for future nanoelectronic applications. We show that the interface resistance in Gr-MoS_2 heterojuctions can affect the overall resistance of the device if the channel (MoS_2) length is small at low carrier densities, whereas, at high carrier densities interface resistance do not play much role in determining the resistance of the entire device. However, if graphene and MoS_2 grains are misorientated then interface resistance can play a crucial role in determining the overall resistance of the device. We also show a weak dependence of misorientation angles on GB resistance across MoS_2 grain boundaries.

TABLE OF CONTENTS

LIST OF FIGURES

Figure **Page**

CHAPTER 1

INTRODUCTION

Over the past few decades, a huge leap in technological progress has been evidenced, most of which can be attributed to the rapid growth of the semiconductor industries. Silicon based technology used in semiconductor industries enabled miniaturization of transistors, which followed a relatively simple rule given by Gordon E. Moore, co-founder at Intel. Moore's prophecy combined with Dennard's scaling rules gave a simple thumb rule to multiply the number of transistors in a chip at an economical rate and governed the semiconductor industries for around 40 years. However, in the last decade or so, Moore's law has come to a saturation, when severe challenges were raised due to continuous scaling of the transistors. The channel length of these modern transistors has already hit the sub-10 nm regime where quantum tunneling of electrons becomes quite significant, which consequently leads to leakage current. Besides electric power management issues, thermal management is also one of the major hindrances, which is putting an upper bound on the shrinking of transistors by Moore's law. Since then there has been a growing thrust in the quest for a new material which can take over the legacy of silicon in the field of semiconductor commerce. Two-dimensional materials like graphene, transition metal dichalcogenides (TMDCs) etc. have shown great promise for many thermal and electrical applications.

Until 2004 it was believed that two-dimensional materials can not exist due to thermal instability, when for the first time graphene was separated from bulk graphite and it was found to possess extraordinary electronic, thermal and mechanical properties. A very high intrinsic mobility in the order of 10^5 $cm^2V^{-1}s^{-1}$ and thermal conductivity of about 5000 $Wm^{-1}K^{-1}$ were reported. These measurements engendered a possibility for the re-

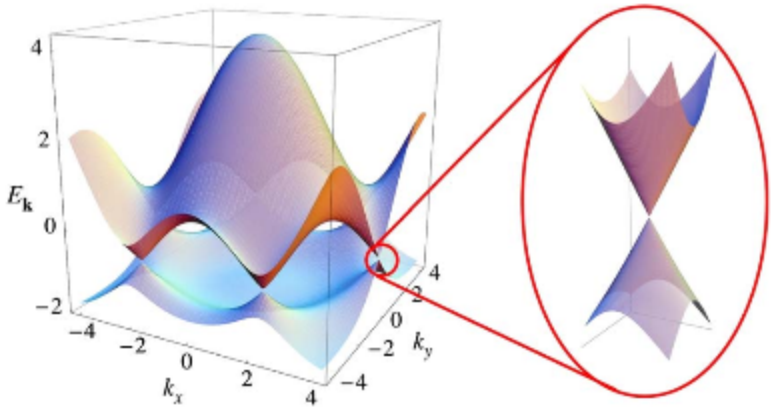

Figure 1.1. Electronic band structure of graphene. Castro Neto et al., The electronic properties of graphene, Rev. Mod. Phys. 81, 109 (2009)

placement of silicon-based technology and thereby resulting into an upsurge in the field of research. Since then, there have been innumerable studies conducted to study the properties of graphene and other two-dimensional materials. In spite of having electron mobility about 100 times greater than that of silicon, graphene doesn't show great promise for future nanoelectronic transistors because of the absence of band gap as can be seen in Fig. 1.1. However, transition metal dichalcogenides such as MoS_2, $MoSe_2$, WS_2 etc. are another class of two-dimensional materials which are semiconductor in nature and have inherent band gap, which makes them a prospective class of material for future nanoelectronic devices.

1.1 Extrinsic factors affecting transport

As discussed earlier, an infinite sheet of single crystalline graphene exhibits very high electronic mobility and thermal conductivity; however when external parameters like size, grain boundaries, substrate, impurities etc. come into play, both thermal conductivity and electronic mobility are affected. This has be schematically represented in Fig. 1.2.

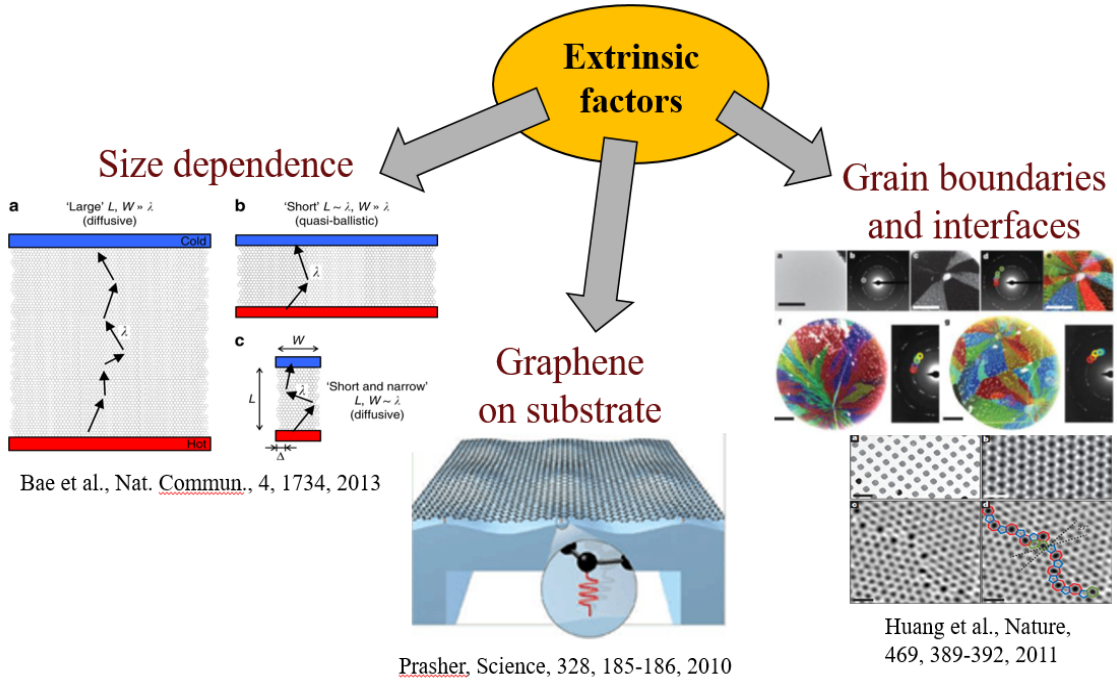

Figure 1.2. Extrinsic factors affecting thermal conductivity

1.1.1 Size dependence on thermal conductivity

A material, where phonon-phonon scattering is strong, shows a smooth ballistic-to-diffusive crossover of heat flow; in such cases, thermal conductivity (K) can be given as $K(L) = (G/A)(L^{-1} + \Lambda^{-1})$, where G/A is conductance (G) per unit area of cross-section (A) of heat flow, Λ is the mean free path of phonons, which is defined as the average distance traversed by phonons between two scattering events. L is the distance between the heat source and sink, which we would refer as length of the system here onwards. For a bulk material where $\Lambda \ll L$, thermal conductivity becomes equal to (G/A)Λ and is therefore independent of length (L) in this diffused regime as shown in the Fig. 1.3. On the other extreme when $L \ll \Lambda$, thermal conductivity becomes proportional to L called the ballistic regime.

However, it has been both experimentally and numerically reported that thermal conductivity in single crystalline graphene shows a logarithmic dependence on L even at lengths far greater than the mean free path of phonons in graphene ($\approx$800 nm). So there

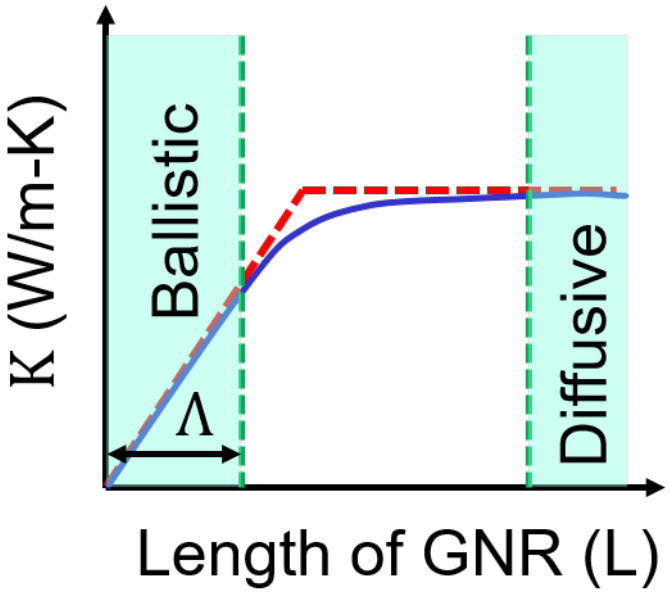

Figure 1.3. General size dependence of thermal conductivity showing ballistic and diffusive regime

has been an intense interest in the research community to unravel the physics behind this anomalous behavior. Besides length, the width and line edge roughness might play an important role in governing thermal transport in two-dimensional systems.

1.1.2 Effect of substrate on thermal conductivity

Thermal conductivity in single crystalline suspended graphene has been reported to vary over a wide range from 1800-5300 $Wm^{-1}K^{-1}$, which is about 10 to 30 times higher than bulk silicon. However it has been found that when graphene is placed on a substrate, thermal conductivity reduces to about 500-600 $Wm^{-1}K^{-1}$. This reduction is being attributed to the suppression of the out-of-plane (ZA) mode due to the substrate. In-plane thermal transport in supported graphene on different substrates such as SiO_2, SiN, boron nitride etc. has been studied in the literature. In chapter 3, we study in-plane thermal transport for graphene with grain boundaries on silicon nitride substrate.

1.1.3 Effect of grain boundaries (GBs) on thermal and electron transport

Two-dimensional materials, in pristine form, showed a great promise due to their high electronic and thermal conductivities. However, it is found to be extremely difficult to fabricate large single crystalline pristine 2-D samples. Most of the large samples are found to be polycrystalline in nature and the conductivity, especially heat conduction, is reduced by about two orders of magnitude due to the presence of grain boundaries (GBs). In recent years there also have been many studies on the effect of GB on electronic transport in two-dimensional structures, however, the effect of grain mismatch angle on electronic transport is not very well understood. Thus in order to effectively use these materials for future electronics and thermal applications, one should develop a stronger understanding of the effect of GBs on transport (both electrical and thermal) in these 2-D materials.

1.2 Outline

In the second chapter, we have studied the effect of finiteness of graphene sheet on its thermal conductivity and added a valuable insight on answering the debatable question about logarithmic divergence of thermal conductivity in suspended graphene ribbons. Grain boundaries (GB), in general, are believed to reduce the thermal conductivity. But correlation of grain mismatch angles with thermal conductivity is not very well understood. In Chapter 3, we report a direct correlation between thermal boundary resistance and mismatch angles across graphene grain boundaries. In the same chapter we also discuss about the possibility of the formation of a disordered patch at grain boundaries and how the width of this disordered patch may be directly related to the mismatch angle. In chapter 4, we show that a lateral heterostructure formed between graphene and MoS_2 exhibits an ohmic-type contact, which can be potentially used for densely-packed future nanoelectronic transistors. Using a novel semi-classical approach, we have computed the interface resistance across in-plane graphene-MoS_2 interfaces. In this work, we assumed that there is no angle mismatch between graphene and MoS_2 grains. In Chapter 5, we study the ef-

fect of the mismatch angle on electronic transport across the interfaces formed between (a) graphene-graphene GBs (b) MoS_2-MoS_2 GBs and (c) graphene-MoS_2 interface.

CHAPTER 2

SIZE DEPENDENCE OF THERMAL CONDUCTIVITY IN GRAPHENE NANORIBBONS

2.1 Introduction

In recent years, 2-dimensional materials have been the subject of intense research because of their unique electronic and thermal transport behavior. Among such materials, graphene has been studied the longest and has shown the most promising properties, with the highest reported thermal conductivity (ranging from 1800-5300 W/m-K) [6, 37, 18] and electron mobility (intrinsic limit in the order of 10^5 cm^2/V-s) [17]. Engineering graphene devices require a firm understanding of thermal transport mechanism, which is mainly dominated by phonons [5, 61] because of strong covalent sp^2 bonding, which efficiently transfers heat by lattice vibrations. Despite enormous progress in understanding the thermal transport in graphene, there are several questions yet to be answered. In 3-dimensional samples, thermal conductivity converges to the bulk value of graphite when the size exceeds the mean free path (mfp) of phonons and transport becomes entirely diffusive in nature. Heat conduction in such a case is mainly governed by resistive umklapp phonon-phonon scattering rather than scattering from the rough boundaries. In contrast, a length dependent behavior of thermal conductivity has been observed in 1-D and 2-D materials even for samples much bigger than mean free path of phonons. There are rigorous mathematical proofs for such diverging behavior in momentum-conserving one-dimensional systems [39, 22, 51, 58] and it has also been experimentally demonstrated for carbon nanotubes [15]. However, in 2-D materials, the reason for this length divergence is still much in debate.

Recently, Xu et al. [65] provided an experimental evidence of this length divergence for samples as long as 9 μm (around 10 times greater than the average mean free path of acoustic phonons in suspended graphene) and attributed the reasons for length divergence to the reduced dimensionality and displacement of in-plane phonon populations at stationary non-equilibrium conditions. In addition, quasi-ballistic propagation of extremely long wavelength acoustic phonons has been demonstrated by Mei et al. [48], where they have shown that about 20$\%$ of phonons have mean free path greater than 100 μm, indicating a wide ballistic to diffusive crossover regime and thermal conductivity ultimately converging to 5800 W/m-K. Nika et al. [52] emphasized the importance of low frequency acoustic phonons, illustrating that with the increase in the sample size, more such low frequency phonons can be excited, which in turn contributes to thermal conduction, thereby leading to length-dependent behavior. Lindsay et al. [41] explained the significance of low frequency ZA phonons towards thermal conductivity in graphene flakes, which leads to length-dependent behavior.

In contrast to the aforementioned studies, Chen et al. [18] reported thermal conductivity in graphene flakes without any sample size dependence. This was attributed to large uncertainty in the measurement of thermal conductivity due to grain boundaries, wrinkles, defects or polymeric residues in the graphene sample. Park et al. [56] used MD simulations to demonstrate the length dependence over a wide range and interestingly, showing a converging behavior of thermal conductivity at 16 μm and finally reporting a macroscopic limit of heat transport in graphene flakes as 3200 W/m-K. Recently, Barbarino et al. [7] performed direct atomistic simulation called approach-to-equilibrium molecular dynamics (AEMD) to capture thermal conductivity in large samples. They found that intrinsic thermal conductivity in monolayer graphene is upper-limited. Thus, there have been both theoretical and experimental evidences of length divergence of thermal conductivity for large samples (up to few microns), but still there has been an active debate going on about the divergence of thermal conductivity for flakes when $\mathrm{L} \longrightarrow \infty$.

In this chapter, we study the length and width dependence of the thermal conductivity of suspended graphene ribbons. In Sec. 2.2 we present the details of the method used to calculate thermal conductivity in graphene ribbons which is based on the full phonon dispersion and the improved Callaway model recently proposed by Allen [3]. In Sec. 2.3 we discuss our results, showing two distinct regimes of thermal transport as the length of the graphene ribbon is increased: logarithmic divergence below 100 μm, driven by the flexural branch, and convergence for lengths exceeding 100 μm caused by renormalization of the flexural branch due to coupling between in-plane and cross-plane phonons in the long wavelength regime. We also show a strong width dependence of thermal conductivity in graphene ribbons due to the non-resistive normal contribution. Finally, in Sec. 2.4 we conclude and comment on the connection of our work to the newly discovered hydrodynamic regime of thermal transport in 2-dimensional materials.

2.2 Theoretical calculations using improved Callaway model

Several techniques have been employed to model thermal transport in graphene such as non-equilibrium molecular dynamics (NEMD), [59, 24] non-equilibrium Green's functions (NEGF) [66, 30] and Boltzmann transport equation simulations. [34, 53, 1] In our work, we have used the solution of full phonon Boltzmann transport equation (pBTE) in order to calculate thermal conductivity in GNRs based on Allen's improved Callaway model. The steady state phonon BTE can be written as

$$\vec{v}(\vec{q},\mathrm{b}) \bullet \nabla_{\vec{r}} N_{\vec{q}} = -\frac{N_{\vec{q}} - N^0_{\vec{q}}}{\tau_C(\vec{q},\mathrm{b})} - \frac{N_{\vec{q}} - N^*_{\vec{q}}}{\tau_N(\vec{q},\mathrm{b})} \tag{2.1}$$

where $N_{\vec{q}}$ is the number of phonons with wave vector $\vec{q}$, $N^0_{\vec{q}}$ is equilibrium Bose-Einstein distribution, $\vec{v}(\vec{q},\mathrm{b})$ is the group velocity and $\tau_C(\vec{q},\mathrm{b})$ is the effective relaxation time due to all scattering mechanisms (which include phonon-phonon scattering, isotope scattering, impurity scattering and edge roughness scattering). Anharmonic phonon-phonon interactions can be categorized into umklapp (U) and normal (N) processes. Umklapp processes

(which destroy crystal momentum) relax the non-equilibrium distribution to the final zero-current equilibrium Bose-Einstein distribution and are resistive in nature whereas N processes conserve crystal momentum and relax the perturbed distribution to a flowing equilibrium ($N^*_{\vec{q}}$). In materials like graphene, where the Debye temperature is very high (about 2100 K) [64, 50], these momentum conserving normal processes have been shown to play a significant role in context of heat conduction [41].

The $N^*_{\vec{q}}$ term represents a flowing equilibrium to which the distribution evolves under the influence of momentum-conserving normal phonon-phonon processes. Flowing equilibrium can be envisioned as a hydrodynamic component [14]—while momentum-destroying resistive processes such as umklapp scattering tend to relax the non-equilibrium distribution back to its equilibrium Bose-Einstein form; the non-resistive normal processes conserve crystal momentum and hence cannot fully destroy the heat flux, but only redistribute it among the phonon modes. Umklapp scattering, isotope scattering and edge roughness scattering all destroy crystal momentum; thus all these resistive processes can be grouped under $\tau_U^{-1}(\vec{q}, \mathrm{b})$. The combined scattering rate is given as the sum of resistive and non-resistive terms ${\tau_C}^{-1}(\vec{q}, \mathrm{b}) = {\tau_U}^{-1}(\vec{q}, \mathrm{b}) + {\tau_N}^{-1}(\vec{q}, \mathrm{b})$, where ${\tau_N}^{-1}(\vec{q}, \mathrm{b})$ is the scattering rate due to normal scattering. The thermal conductivity expression includes an extra term over the Debye term and is called N-drift term, which accounts for additional conductivity from the non-resistive normal processes so that $K_{tot} = K_C + K_N$.

Allen[3] improved the Callaway model [13] and proposed a modified expression in order to correctly include the contribution of resistive (processes which destroy crystal momentum) and non-resistive (which conserves crystal momentum) processes towards thermal conductivity and added a correction term $\left(\frac{\lambda_1 \lambda_2}{\lambda_3}\right)$, summed over all the branches b, to the Debye term K_C. The accuracy of the improved Callaway model (ICM) was compared with the iterative solution of the BTE by Ma et al. [44], to find that the trend of lattice thermal conductivity against temperature obtained from the ICM compares more favorably

to the full iterative BTE solution than the RTA or the original Callaway model, especially in those cases where normal scattering is significant.

The modified ICM expressions are given as:

$$K_{tot} = K_C + K_N = K_C + \sum_{\mathrm{b}} \frac{\lambda_{1,\mathrm{b}}\lambda_{2,\mathrm{b}}}{\lambda_{3,\mathrm{b}}} \tag{2.2}$$

where K_C is the Debye term, arising from relaxation time approximation (RTA) and sometimes also called as K_{RTA}, and is given by

$$K_C = \frac{1}{A\delta} \sum_{\vec{q},\mathrm{b}} \hbar\omega_{\vec{q},\mathrm{b}} v_{\parallel}^2(\vec{q},\mathrm{b}) \tau_C(\vec{q},\mathrm{b}) \frac{\partial N_{\vec{q}}}{\partial T} \tag{2.3}$$

where A is the area of GNR sheet, δ (=0.335 nm) is thickness of graphene monolayer[40] and the correction terms can be expressed as:

$$\lambda_{1,\mathrm{b}} = \frac{1}{A\delta} \sum_{\vec{q}} v_{\parallel}(\vec{q},\mathrm{b}) q_{\parallel} \tau_C(\vec{q},\mathrm{b}) \frac{\partial N_{\vec{q}}}{\partial T} \tag{2.4}$$

$$\lambda_{2,\mathrm{b}} = \frac{1}{A\delta} \sum_{\vec{q}} v_{\parallel}(\vec{q},\mathrm{b}) q_{\parallel} \left[\frac{\tau_C(\vec{q},\mathrm{b})}{\tau_N(\vec{q},\mathrm{b})}\right] \frac{\partial N_{\vec{q}}}{\partial T} \tag{2.5}$$

$$\lambda_{3,\mathrm{b}} = \frac{1}{A\delta} \sum_{\vec{q}} \left(\frac{q_{\parallel}^2}{\hbar\omega_{\vec{q},\mathrm{b}}}\right) \left[\frac{\tau_C(\vec{q},\mathrm{b})}{\tau_U(\vec{q},\mathrm{b})}\right] \frac{\partial N_{\vec{q}}}{\partial T} \tag{2.6}$$

The expression for resistive umklapp scattering rate is taken from the work of Slack et al. [49] and is given as $\tau_U^{-1}(\vec{q},\mathrm{b}) = B_U \omega_{\vec{q},\mathrm{b}}^{a_U} T^{b_U} e^{-\theta_{\mathrm{b}}/3T}$, where $\overline{v}_{\mathrm{b}}$ is velocity of sound for each branch b and is calculated by average slope of its dispersion curve near Γ point [36], γ_{b} is the Gruneisen parameter, θ_{b} is the Debye temperature of each phonon branch, $\overline{M}$ is the average atomic mass of carbon and $B_U = \frac{\hbar\gamma_{\mathrm{b}}^2}{\overline{M}\theta_{\mathrm{b}}\overline{v}_{\mathrm{b}}^2}$, for a_U and b_U equal to 2 and 1 respectively, which have been used in innumerable studies conducted so far and produced excellent results.

An empirical form for normal scattering has been adopted from the paper by Slack et al. [49]: $\tau_N^{-1}(\vec{q},\mathrm{b}) = B_N \omega_{\vec{q},\mathrm{b}}^{a_N} T^{b_N}$, where

$$B_N(a_N, b_N) = (k_B/\hbar)^{b_N} \frac{\hbar \gamma_{\mathrm{b}}^2 v^{(a_N+b_N-2)/3}}{\overline{M} v^{a_N+b_N}} \tag{2.7}$$

This simple model allows us to efficiently study a broad range of sizes and temperatures with good accuracy. Several studies have been carried out to determine the best empirical values for the constants a_N and b_N, which can accurately describe the contribution from momentum-conserving normal processes. For our study, we have used a_N and b_N to be 1 and 3 respectively, which has been used in several studies to explain the contribution from normal processes in materials like diamond [54] and LiF [10] and fits experimental as well as first principle data in quite good agreement. In particular, first principles calculations predict a constant ($a_N = 0$) frequency dependence in pristine graphene; however, the constant dependence of the anharmonic scattering rate on phonon frequency was found to disappear in the presence of strain [11]. Even infinitesimally small amounts of strain were found to lead to a quadratic ($a_U = 2$) dependence for in-plane LA and TA branches and linear ($a_N = 1$) for flexural ZA branch. This linear dependence can be also tied to the maximum scattering rate in the long wavelength limit. In long wavelength limit ($\omega \to 0$), the upper bound on the phonon scattering rate ($\Gamma_{max} = 1/\tau_{min}$) is dictated by the Ioffe-Regel limit [28]; equivalently, it can be obtained from Cahill's minimum thermal conductivity model [12], according to which $\omega\tau_{min} = \pi$. In addition, as pointed out by Bonini et al. [11], for the quasi-particle criterion ($\omega\tau \geq 1$) to hold, the exponent a_N in $\tau_N^{-1}(\vec{q},\mathrm{b}) \propto \omega_{\vec{q},\mathrm{b}}^{a_N}$ has to be greater than or equal to 1 in the long wavelength limit.

Naturally occurring isotopes of carbon can result in scattering due to difference in their atomic masses. Thus, isotope scattering is also included while calculating the effective scattering rate and is given as [1]: $\tau_{Iso}^{-1}(\omega) = (\Gamma\Omega_0/12)\omega^2 g(\omega)$, where the effective density of states is calculated by summing the density of states over all the branches b; $g(\omega) = \sum_{\mathrm{b}} g_{\mathrm{b}}(\omega)$. The mass-difference constant Γ is given by $\Gamma = \sum_i f_i(1 - M_i/\overline{M})^2 = c(1 -$

$c)/(12-c)^2$. The natural abundances of C^{12} and C^{13} are 98.9% and 1.1% respectively and thus, c= 0.011.

In graphene nanoribbons, boundaries start playing a significant role in scattering of the heat carriers. As the edges of GNRs are not perfectly smooth, thus phonons tend to scatter from the boundaries and this effect becomes prominent with increase in rms value of edge roughness and decreased width of nanoribbons. In this work, the scattering rate due to line edge roughness (LER) is calculated in the same way as was done by Aksamija and Knezevic [2]. A momentum-dependent specularity parameter $p(\vec{q}) = exp(-4q^2\Delta^2 sin^2\theta_E)$ has been introduced in order to accurately treat phonon scattering from edge roughness. It represents the ratio of specular reflections to the total number of interactions with the boundary. Δ represents rms value of the line edge roughness and θ_E represents the angle made by incident phonons ($\vec{q}$) with the edge direction. The final expression for an effective LER scattering rate is given by [2]

$$\tau_{LER}^{-1}(\vec{q},\mathrm{b}) = \frac{v_{\perp}(\vec{q},\mathrm{b})}{W}F_p(\vec{q})\Bigg/\left[1-\frac{\Lambda_{int.}^{\perp}(\vec{q},\mathrm{b})}{W}F_p(\vec{q})\right] \tag{2.8}$$

where $\Lambda_{int.}^{\perp}(\vec{q},\mathrm{b}) = v_{\perp}(\vec{q},\mathrm{b})\tau_{int.}(\vec{q},\mathrm{b})$ is the phonon mean free path due to all the intrinsic processes. The complex interplay between line edge roughness scattering and internal scattering mechanisms for graphene ribbons is encapsulated in the parameter $F_p(\vec{q})$ called the form factor

$$F_p(\vec{q}) = \frac{[1-p(\vec{q})]\left[1-exp\left(-W/\Lambda_{int.}^{\perp}(\vec{q})\right)\right]}{1-p(\vec{q})exp[-W/\Lambda_{int.}^{\perp}(\vec{q})]}. \tag{2.9}$$

Contacts are assumed to be ideal and in equilibrium, which is captured by treating the interaction of phonons with the contacts analogously to the interaction of phonons with completely diffuse edges ($p(\vec{q}) = 0$) except having width (W) replaced by length (L) and the component of the phonon group velocity being taken along, rather than across, the ribbon. Thus, a length dependent scattering term is given as $\tau_{end}^{-1}(\vec{q},\mathrm{b}) = v_{\parallel}(\vec{q},\mathrm{b})/L\left[1-\exp\left(L/\Lambda_{int.}^{\parallel}(\vec{q})\right)\right]$.

The scattering rates (normal, umklapp, isotope and edge roughness) are added to get total combined rate in suspended graphene as

$$\frac{1}{\tau_C(\vec{q},\mathrm{b})} = \frac{1}{\tau_U(\vec{q},\mathrm{b})} + \frac{1}{\tau_N(\vec{q},\mathrm{b})} + \frac{1}{\tau_{Iso}(\omega)} + \frac{1}{\tau_{LER}(\vec{q},\mathrm{b})} + \frac{1}{\tau_{end}(\vec{q},\mathrm{b})} \tag{2.10}$$

and thus, can be used to calculate the resistive Debye term K_C and the non-resistive normal contribution K_N of thermal conductivity in GNRs.

2.3 Results and Discussion

The size dependence of thermal conductivity in GNRs has been studied under two separate headings in this work —(a) Length dependence (b) width dependence of thermal conductivity.

2.3.1 Length dependence of thermal conductivity

To study length dependence of thermal conductivity at room temperature, we scaled ribbon length while keeping the width constant (W=1.5 μm) in order to mimic the experimental set-up by Xu et al. [65]. In Fig. 2.1(a), thermal conductivity of free-standing graphene has been plotted against length for various discretization densities of the phonon dispersions. The red curve in Fig. 2.1(a) shows a convergence in thermal conductivity for a coarse discretization of q-points having 100,000 points in the first Brillouin zone. Previous studies suggest that a major part of thermal conductivity comes from the quadratic out-of-plane ZA modes and divergence is a consequence of long wavelength problem. Klemens [33] was among the first to propose a logarithmic divergence of thermal conductivity in the two-dimensional phonon gas. In his simplified umklapp-limited model, the spectral specific heat (C(ω)) in two dimension is proportional to ω while the intrinsic mean free path $l_i(\omega) \propto \omega^{-2}$T assuming a quadratic umklapp scattering rate and linear dispersion. Klemens then attributed the logarithmic divergence to the problem of long waves: in the limit q$\rightarrow$0, as the phonon wavelength gets larger; the spectral phonon density

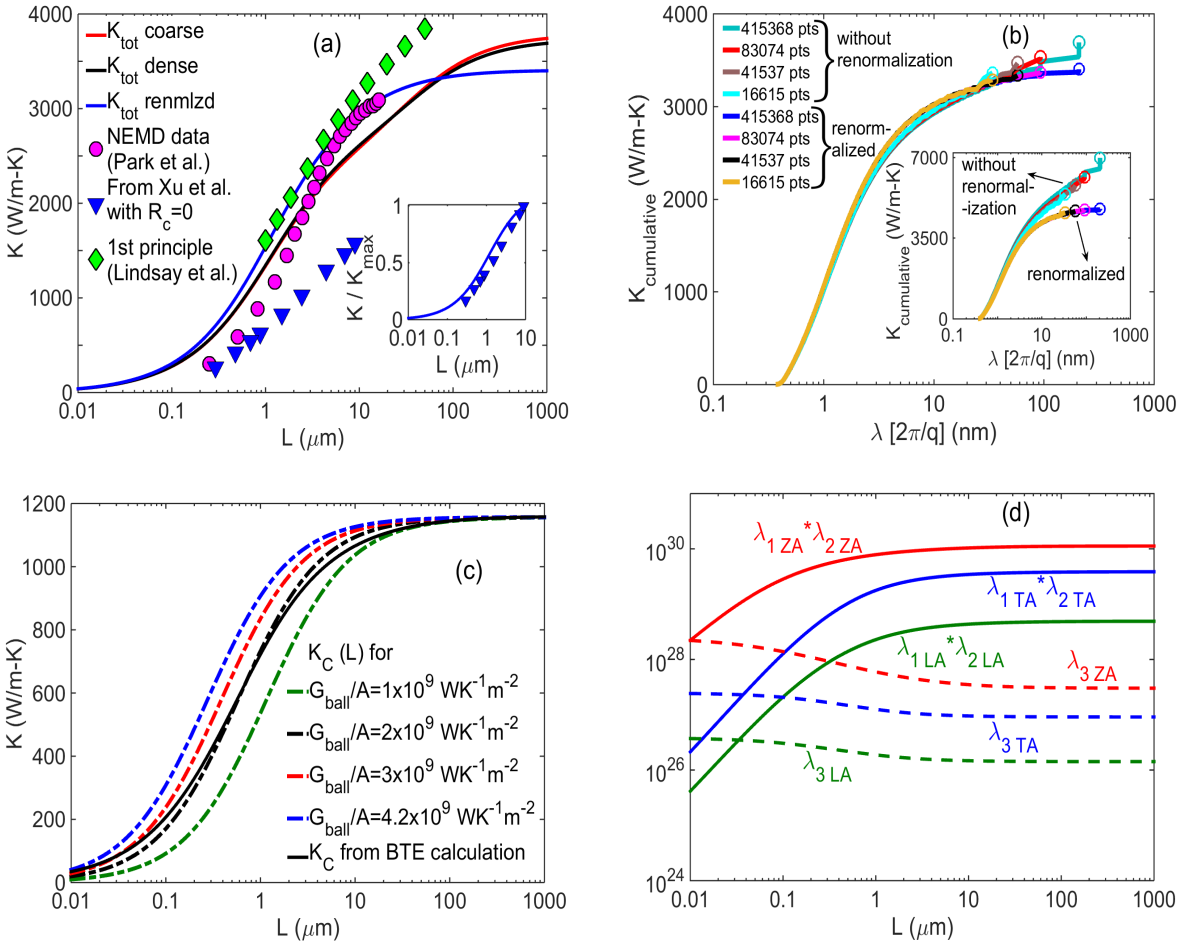

Figure 2.1. **(a)** Convergence of thermal conductivity ($K_{tot} = K_C + K_N$) with length (L). Red and black solid lines in both **(a)** and **(b)** (coincide for most of the part) represent K_{tot} for coarse and denser discretization grid respectively with quadratic ZA modes while blue solid line in both **(a)** and **(b)** shows convergence of thermal conductivity for denser discretization grid with renormalized ZA dispersion. Diamond (in cyan) and circular (in magenta) markers represent first principle data from Lindsay et al.[41] and non-equilibrium MD (NEMD) simulation data from Park et al.[56] respectively. (Inset) Comparison of our normalized thermal conductivity (blue solid line) with the normalized experimental data (blue triangles) for zero contact resistance from Xu et al.[65]. **(b)** Cumulative K_{tot} from different phonon wavelength. **(c)** Compares resistive thermal conductivity (K_C represented by black solid line) from our BTE calculations with K_C(L) (resistive thermal conductivity as a function of L represented by dash-dot lines) calculated from simple 'gray' approximation[4] by fitting different $G_{ballistic}/A$ values. **(d)** Branchwise contribution of the correction factors in K_N ($\sum_\lambda \frac{\lambda_1 \lambda_2}{\lambda_3}$). For **(a)**-**(d)** Width and rms value of edge roughness (LER) used are 1.5 μm and 2 nm respectively and temperature is 300 K.

($N(\omega) = n_0(\omega)g(\omega) \propto 1/\omega$) diverges, leading to a logarithmic divergence in the resulting thermal conductivity integral [40].

In order to treat the problem of long waves more accurately, we repeated our calculation of thermal conductivity keeping all parameters exactly the same, but employing a much denser discretization grid of q-points having 400,000 points for the dispersion and numerical integration. We obtained a similar converging behavior as shown by the black curve in Fig. 2.1(a). To further study the convergence in long wavelength limit, we plotted the cumulative thermal conductivity as a function of phonon wavelength, as shown in Fig. 2.1(b). In both the cases (red and black curves representing coarse and denser discretization grids, respectively), steps can be observed at the largest wavelength in the discretization, indicating an increase in thermal conductivity due to the addition of more long wavelength phonons. Despite the addition of more discretization q-points around q$\longrightarrow$0 by making the dispersion grid denser, the results still do not converge fully. However, the size of the last step in the black curve (denser grid) decreases relative to the red curve (coarser grid), indicating that convergence is slow and would require even denser grids. We conclude that the convergence observed in Fig. 2.1(a) is not an actual convergence but rather a numerical one, caused by the finite number of discretization points. Thus our results show that even for a ribbon with fixed width and diffuse edges, thermal conductivity diverges with length as long as the dispersion of the out-of-plane ZA modes is quadratic.

However, several recent studies have shown that increasing the size of the free-standing graphene will gradually cause a stiffening of the flexural modes, arising out of the coupling between in-plane and out-of-plane modes. This coupling has been found to result in renormalization of ZA modes. The blue curve in Fig. 2.1(a) and Fig. 2.1(b) represents thermal conductivity with dense discretization grid with renormalized ZA dispersion (renormalization will be further discussed in the next section). This stiffening of ZA modes causes convergence of thermal conductivity with length and leads to a finite value of thermal conductivity, as evidenced by the smooth convergence and the lack of large steps in the long

wavelength limit (Fig. 2.1(b)). Good agreement between our result (solid blue line) with previously reported first principles [41] (cyan-colored diamond markers in Fig. 2.1(a)) and molecular dynamics [56] calculations (magenta-colored circular markers in Fig. 2.1(a)) confirm that the improved Callaway model can be used as an effective tool for the treatment of momentum-conserving normal processes. Our calculated thermal conductivity, when scaled with K_{max} to compensate for contact resistance in the experiments, follows the same trend as that of the measured data [65], shown in the inset of Fig. 2.1(a).

Here, the analysis of the divergence of thermal conductivity with length is generalized to include the quadratic dispersion of the ZA branch and the non-resistive normal contribution, both of which were ignored in previous analyses. For a general dispersion of the form $\omega \propto q^s$, frequency dependence of the group velocity ($\vec{v}(\vec{q}) = \nabla\omega(\vec{q})$) is given as $v \propto \omega^{(s-1)/s}$ while the density of states $\mathrm{D}(\omega) \propto \omega^{(2-s)/s}$. In the long wavelength limit ($\omega \longrightarrow 0$) and for finite width, the resistive part of thermal conductivity (K_C) is mainly dominated by edge roughness scattering which, according to equation 2.8, varies as $\tau_{LER}^{-1}(\omega) \propto v(\omega)$. Thus the resistive part of thermal conductivity ($K_C(\omega)$) $\propto v^2(\omega)\tau_{LER}D(\omega) \propto \omega^{(1/s)}$ indicating that K_C converges with length and reaches the diffusive regime as long as we maintain finite width of the samples, irrespective of the value of the exponent s, as our results in Fig. 2.1(c) indicate.

The length dependence of the resistive component of thermal conductivity (K_C) can be captured through a simple Landauer model [57, 31], where the heat conduction is described by constant thermal conductance (G) in the ballistic regime. Then the length variation in K_C is well described by a transition from the ballistic to the diffusive regime as $K(L) = [A/(LG_{ball}) + 1/K_{diff}]^{-1}$ [4]. Setting (G_{ball}/A)=2$\times 10^9$ $WK^{-1}m^{-2}$ exactly fits the resistive part of thermal conductivity as shown in Fig. 2.1(c). The mean free path (λ) is calculated from this value by angle averaging in 2D as $K_{diff} = (G_{ball}/A)(\pi/2)\lambda$. The mfp of phonons in suspended graphene with rough boundaries and W=1.5 μm is thus calculated to be 358 nm, somewhat smaller than previously reported values of around 800 nm

for large square samples [25] due to the presence of edge roughness of 2 nm in our case. Hence we conclude that the resistive contribution to the thermal conductivity is undergoing a simple ballistic-to-diffusive transition as length is increased, saturating when L>10 μm.

On the other hand, the length dependence of thermal conductivity of long ribbons (L>1 μm) is dominated by the hydrodynamic contribution, represented by K_N, and its length dependence is different from what can be observed in ballistic regime. The non resistive normal contribution (K_N) is comprised of the three factors: λ_1, λ_2 and λ_3, where, by analysis analogous to that for K_C, we find that $\lambda_2 \propto \omega^{(3-s)/s}$ and $\lambda_3 \propto \omega^{(5-2s)/s}$ (based on Eqs. 2.5 and 2.6). Thus for $s \leq$2.5 both λ_2 and λ_3 will converge with increasing length. However, $\lambda_1 \propto \omega^{(3-2s)/s}$ and thus, for a purely quadratic dispersion (s=2), thermal conductivity will not converge even in the presence of edge roughness. This is evident in Fig. 2.1(b) where red and black curves show a continuing step behavior as length is increased; we obtain a finite value only because our discretization is finite and length eventually exceeds the largest phonon wavelength captured in the long wavelength limit.

As we noted earlier, Mariani and von Oppen [46] reported that increasing the size of the graphene sheet leads to stiffening of the flexural modes due to the coupling force between bending and stretching degrees of freedom, thereby causing renormalization of flexural modes as $\omega_{ZA} = \beta_{ZA}(q)q^2$ where $\beta_{ZA}(q) = \alpha_{ZA}[1+(q_c/q)^2]^{1/4}$, q_c being the cut-off wavevector. The temperature dependent transition point q_c is calculated to be 0.1 (in the units of 2π/lattice constant) [46]. When L$\rightarrow \infty$ (q$\rightarrow$0), $q_c \gg$q and ω_{ZA} becomes proportional to $q^{3/2}$. Renormalization of ZA modes and their partial linearization in the long wavelength regime (where s=3/2) causes λ_1 ($\propto \omega^{(3-2s)/s}$), λ_2 ($\propto \omega^{(3-s)/s}$) and λ_3 ($\propto \omega^{(5-2s)/s}$) all to converge with length, as can be seen in Fig. 2.1(d). Therefore the non-resistive normal contribution (K_N) eventually converges to a finite value owing to the coupling between the in-plane and out-of-plane degrees of freedom. The solid blue curve in Fig. 2.1(a) and Fig. 2.1(b) show convergence of thermal conductivity with length to a bulk value of 3400

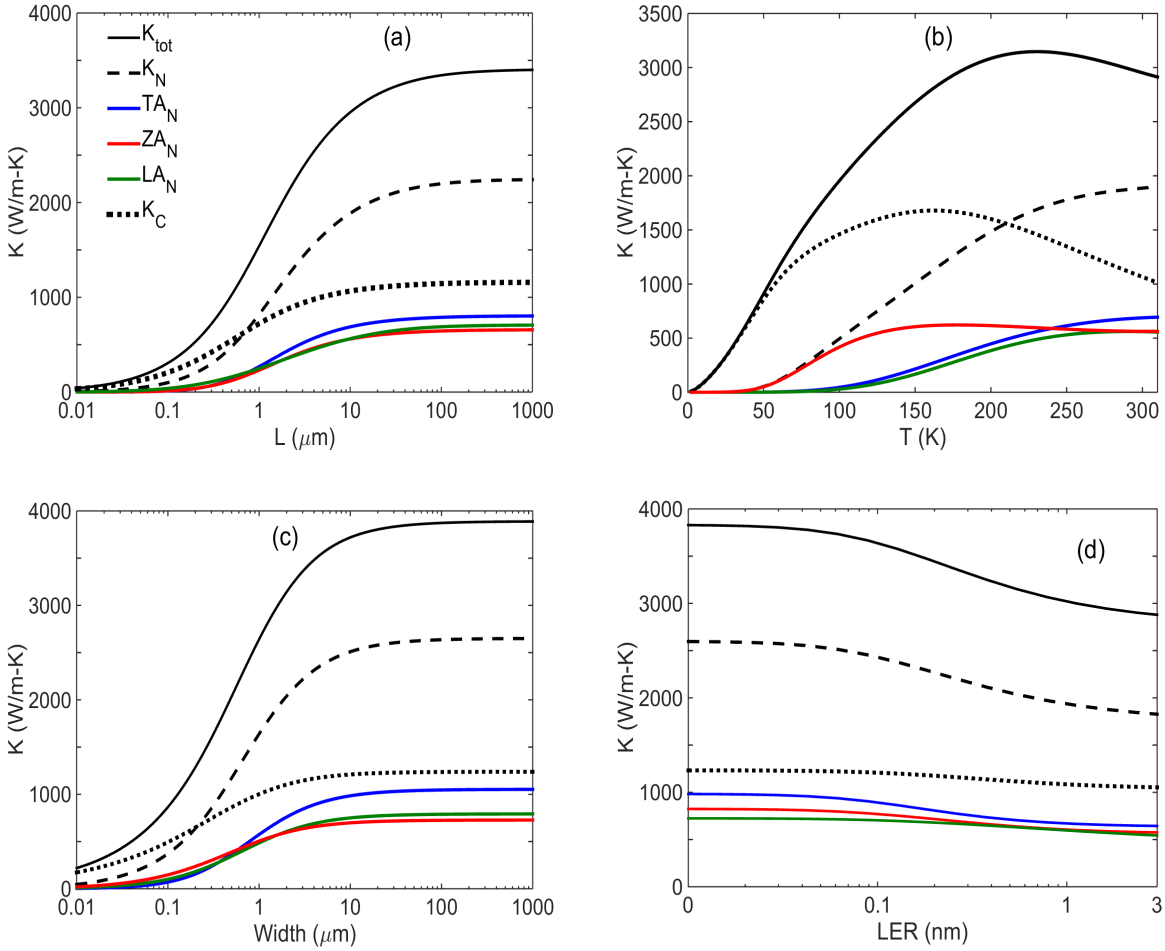

Figure 2.2. **(a)** Branchwise contribution of thermal conductivity against length (L) of GNRs. Black solid and dashed lines (in **(a)**-**(d)**) represent total thermal conductivity $(K_{tot} = K_C + K_N)$ and non-resistive normal contribution (K_N) respectively and black dotted lines ((in **(a)**-**(d)**) represent resistive contribution (K_C). Blue, green and red curves ((in **(a)**-**(d)**) represent TA, LA and ZA components of K_N respectively. **(b)** Effect of temperature on contribution of K_{tot}, K_C and K_N. **(c)** shows width dependence of K_{tot}, K_C and K_N. **(d)** represents the effect of edge roughness on K_{tot}, K_C and K_N. Length of GNRs (in **(b)**, **(c)** and **(d)**) is 10 μm, Width (in **(a)**, **(b)** and **(d)**) is 1.5 μm and temperature (in **(a)**, **(c)** and **(d)**) is 300 K.

W/m-K for ribbon width of 1.5 μm, in good agreement with both experimental measurements and first principles calculations.

Fig. 2.2(a) shows branchwise components of thermal conductivity and their length dependence. Earlier studies have shown that length divergence in thermal conductivity is

due of quadratic dispersion of out-of-plane modes, however because of the coupling between the in-plane and flexural modes renormalization of ZA dispersion takes place, which leads to partial linearization of flexural modes and thereby causes thermal conductivity to converge when L$\rightarrow \infty$ in long wavelength limit. We observe here that the divergence in K_N beyond 10 μm is driven by the out-of-plane ZA branch, but renormalization of the ZA branch prevents λ_1 (Equation 2.4) from diverging (for s=3/2, $\lambda_1 \propto \omega^{(3-2s)/s}$= constant) and the hydrodynamic component eventually reaches saturation for $L >$100 μm, indicating the onset of the Ziman regime where extrinsic effects such as length no longer play a role.

We assumed a sample of 10 μm long and 1.5 μm wide to study the effect of temperature and line edge roughness (LER) on thermal conductivity in graphene ribbons. In Fig. 2.2(b), thermal conductivity (K_{tot}) along with its resistive (K_C) and non-resistive normal components (K_N) are plotted against temperature. At low temperatures, thermal conductivity is mainly comprised of resistive contribution while at room temperature and above, the resistive contribution is suppressed considerably due to strong umklapp phonon-phonon scattering and non-resistive normal contribution starts playing an important role. Thus in graphene, K_C fails to capture the contribution coming from momentum-conserving normal processes and leads to under-evaluation of thermal conductivity at and above room temperatures. It can also be seen that at low temperatures, the out-of plane (ZA) modes coming from K_C contribute significantly to thermal conductivity whereas at high temperatures, most of the conductivity comes from the hydrodynamic contribution (represented by K_N) of the in-plane branches (LA and TA).

2.3.2 Width dependence of thermal conductivity

Next we turn to the width dependence of thermal conductivity in suspended graphene ribbons at room temperature and vary the width W while keeping L=10 μm and a constant edge roughness Δ=2 nm, which puts the ribbons in the fully diffusive edge scattering regime. It can be seen in Fig. 2.3.1(c) that the resistive part of thermal conductivity (K_C)

shows a gradual width dependence. It is because for ribbons narrower than 200 nm, the ribbon is in the ballistic regime where both K_C is suppressed by line edge roughness (LER) scattering ($\tau_{LER}^{-1} \propto$ 1/W). In this range, the contribution from non-resistive processes (K_N) is also significantly reduced by the presence of resistive LER scattering, whereas widths above 200 nm put the ribbon in the Poiseuille regime [38]. In the Poiseuille flow range, where 200 nm$\leq W \leq$10 μm, the K_N is affected by the interplay of LER scattering and normal scattering, leading to a pronounced width dependence exceeding that of the resistive component. The contribution of the non-resistive normal processes to width dependence has not been previously reported and can be understood as a consequence of the hydrodynamic phonon transport suggested by Lee et al. [38]. Beyond 10 μm, K_N transitions into the Casimir regime where normal processes dominate over resistive LER scattering and the thermal conductivity again converges to a finite value.

Unlike their supported counterparts, LER scattering plays a very crucial role in the thermal conductivity of suspended graphene ribbons. Fig. 2.2(d) shows a strong dependence of thermal conductivity (K_{tot}) for edge roughness up to 0.5 nm (rms value). In this figure, it can be seen that K_{tot} corresponding to zero edge roughness is same as that of K_{tot} for 1000 μm wide ribbon as can be seen in Fig. 2.2(c), which again indicates that for such wide ribbons the effect of edge roughness completely dies off. The effect of edge roughness and width of the ribbons can not be completely decoupled. As we keep on reducing the width of the ribbon from 1000 μm with fixed edge roughness is equivalent to increasing the edge roughness for a given width of the ribbon. K_N shows a strong LER dependence up to 0.5 nm whereas K_C shows weaker dependence on edge roughness as is the case for width dependence of thermal conductivity.

2.4 Conclusion

In conclusion, we have studied the length divergence of suspended graphene ribbons, employing the newly developed improved Callaway model to accurately capture the signifi-

cant contribution from the non-resistive normal processes in the hydrodynamic regime. We have shown through both numerical and analytical calculations that this non-resistive normal contribution dominates the length dependence for lengths greater than 1 μm and leads to a logarithmic divergence, even in ribbons with fixed width and edge roughness. This divergence is caused by the combination of the quadratic dispersion of the out-of-plane ZA phonon branch in the long wavelength limit.

However, for lengths exceeding 100 μm, we find that thermal conductivity converges to a constant value. This convergence is independent of width and not caused by edge disorder; rather, it is due to linearization of the ZA branch by coupling between the in-plane and out-of-plane degrees of freedom. This coupling removes the quadratic dependence of the ZA dispersion and limits the normal contribution of the ZA branch to a finite value. We also uncover a prominent width dependence arising from the non-resistive normal contribution for widths exceeding 200 nm, which delineates the emergence of Pouiselle hydrodynamic heat flow. Our study confirms the role of non-resistive normal processes in the length and width scaling of thermal conductivity and provides quantitative limits to the hydrodynamic regime of heat flow in graphene ribbons.

CHAPTER 3

EFFECT OF GRAIN MISMATCH ANGLE ON THERMAL CONDUCTIVITY IN CVD-GROWN GRAPHENE

3.1 Introduction

As discussed in chapter 1, thermal management in nanoelectronic devices is one of the major problems faced by the present semiconductor industry to achieve further miniaturization of transistors. 2-D materials have shown a great potential for future electronics devices due to their high electronic and thermal properties. Graphene has served as a model 2D system for more than a decade now. Large-scale manufacture of graphene for commercial purposes are mostly done by chemical-vapor deposition (CVD) technique. However, CVD-grown graphene are mostly polycrystalline in nature and grain boundaries are found to significantly reduce thermal conductivity in graphene ribbons. So, in order to efficiently dissipate heat in modern electronic devices, it is of utmost importance that we understand the physics behind heat transfer across grain boundaries. A wide range of studies have been conducted to study electronic conduction across grain boundaries of graphene [35, 68, 19, 63]. However, owing to the significance of graphene grain boundaries, a limited range of research has been done to study its effects in determining thermal conductivity across such grain boundaries. Experimental studies suffer from the problem that they require a suitable platform capable of separating grain boundary contribution from the graphene grains itself. On the other hand, in order to theoretically study heat conduction across the interface, the currently available models —acoustic mismatch model (AMM) and diffused mismatch model (DMM) — are not universally effective for predicting thermal boundary resistance, except at very low temperatures. Both models differ

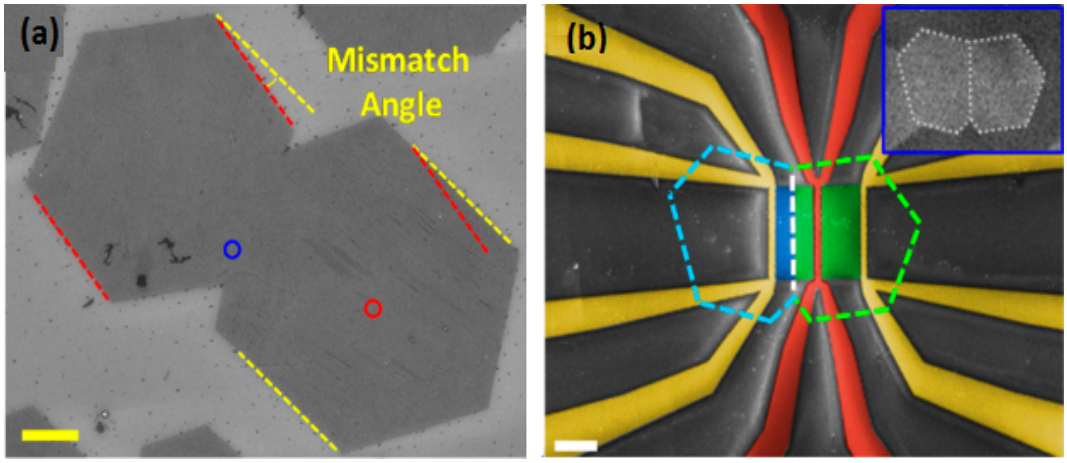

Figure 3.1. **(a)** shows scanning electron microscopy (SEM) image of two merged hexagonally shaped single crystalline graphene grains forming an individually grain boundary (GB). The scale bar is 5 μm. **(b)** High-magnification image of a fabricated thermometry platform comprised of a heater electrode in the center and two sensor electrodes on the sides having perfect symmetry. The scale bar is 5 μm [67].

greatly in their treatment of scattering at the boundary. In AMM the interface is assumed to be perfect, resulting in specular reflection, thus phonons propagate elastically across the interface. The wavevectors that propagate across the interface are determined by conservation of momentum. On the other hand in DMM, the interface is assumed to be perfectly scattering. In this case the incident wavevectors are completely randomized on transmission across the interface and are independent of incident phonons. In both the models the detailed balance must still be obeyed. For most of the materials, AMM and DMM mark the upper and lower limit of thermal conductivity.

In spite of studying thermal conductivity in graphene for more than a decade now, still there isn't any study reporting a direct correlation between thermal grain boundary resistance and grain mismatch angle. In this study, our collaborators fabricated CVD-grown graphene samples in which two graphene flakes were merged to form an individual grain boundary on SiN substrate with a grain mismatch angle between them as shown in the Fig. 3.1(a). The misorientation angles between the grain boundaries in the fabricated samples were measured to be 3°, 8° and 21°. In Fig. 3.1(b), it can be seen that at the center

there is a heater (represented in red) with two sensors, each on either side of the heater (and is represented by yellow lines), placed symmetrically. This configuration allows to study thermal conductivity of graphene grains without any boundaries on right hand side of the figure; whereas on the left hand side the two single crystalline graphene grains are separated by an individual grain boundary (represented by white dashed line).

3.2 Theoretical modelling of thermal transport across graphene GB

The primary carriers of heat in graphene are phonons. Fourth nearest neighbor force constant model, as described by Saito [60], has been used to calculate phonon dispersion. Phonon dispersion of an isolated sheet has been considered for this study, which is a good approximation [55]. The model used for this study is based on the complete solution of phonon Boltzmann transport equation (pBTE) same as used in Chapter 2 and is given by the eqn. 2.1. However, we ignore the second collision term involving normal scattering here because the presence of substrate completely kills off the normal contribution and eqn. 2.1 can be approximated as—

$$\vec{v}(\vec{k})\vec{\nabla}_{\vec{r}}N(\vec{r},\vec{k}) = -\frac{N(\vec{r},\vec{k}) - N_0(\omega,T)}{\tau_i(\omega)} \tag{3.1}$$

where $N_0(\omega,T)$ is equilibrium Bose-Einstein distribution and $\tau_i(\omega)$ is the phonon relaxation time, which can be written as inverse of the total scattering rate. The competing scattering rates comprise of anharmonic interaction of 3-phonon processes (both normal and umklapp), line edge roughness, 1.1 % of C_{13} isotope concentration [2] and surface roughness. Thermal transport in supported graphene ribbons is characterized by the complex interplay between GB roughness scattering and various internal scattering mechanisms (substrate, phonon-phonon, impurity, isotope scattering). It has been studied that in wide supported GNRs, substrate scattering plays a dominant role over line edge roughness scattering [2]. The interaction with silicon nitride substrate is modeled through perturbations to

the scattering Hamiltonian in the same way as was done by Aksamija et al. [2] for graphene on SiO_2. As silicon nitride is a smoother substrate than that of SiO_2, thus, a very low value of force constant for out-of-plane modes (0.011 N/m) has been considered to capture the weak van der Waals coupling force between silicon nitride substrate and graphene. In this model, two-dimensional graphene sheet is considered to be in contact with the substrate in the form of small circular patches with radius of 16.3 nm. To calculate in-plane thermal conductance across graphene grain boundaries, we use the full solution to pBTE in the presence of GBs—

$$K(T) = \frac{\hbar}{S\delta} \sum_{\vec{k},b} v_b^2(\vec{k}) \tau_{tot}(\vec{k}) \omega_b(\vec{k}) \frac{\partial N_0(\omega, T)}{\partial T} \tag{3.2}$$

where S is the surface area of the unit cell, δ=0.335 nm is the graphene thickness, ω_b is the vibrational frequency, and v_b is the group velocity of phonon branch b, computed from the full phonon dispersion relationship.

CVD graphene grows isotropically outwards from each nucleation point until two adjacent single-crystalline grains meet each other and they form the grain boundary. The shape of the boundary, thus formed, depends on the angle of grain mismatch. Small mismatch angles can be envisioned as simple line defects (LD) with a small rms value of grain boundary roughness roughness. But in case of samples with large grain boundary mismatch angle, the boundary can no longer be assumed to be a line defect. Thus, in order to include this additional resistance due to large angle mismatch of GBs, a strip of disordered (amorphous) graphene, whose width is negligible in case of small angles and gradually increases with angle of mismatch, has been considered. The thermal conductivity due to this amorphous region (K_{min}) has been calculated from Cahill′s minimum thermal conductivity model [12], according to which minimum thermal conductivity is reached when the scattering rate is maximum i.e. when scattering rate equals twice the phonon vibrational frequency ($\tau_D^{-1}(\omega) = \frac{\omega}{\pi}$). Equivalently, all the energy of the phonon normal mode

is transferred out during one half of the vibration period, resulting in the relaxation time being equal to half of the period of vibration. In the long wavelength limit, this also implies the mean free path reaches its smallest possible value which is equal to one half of the phonon wavelength $\Lambda_b(q) = v\tau_b(q) = v\frac{\pi}{\omega(q)} = v\frac{\pi}{vq} = \frac{\lambda}{2}$ where λ is the phonon wavelength. Using the disorder scattering rate, thermal conductivity of the disordered region is calculated from eqn. 3.2. Finally the total thermal conductivity of the sample is given as $K_{GB-Region} = \frac{W_G}{(R_{GB-Region}).A}$, where $R_{GB-Region}$ = resistance of the sample in the presence of grain boundary roughness $[(W_G - W_D)/(A.K_G)]$ + resistance due to disordered region $[(W_D)/(A.K_{min})]$, where W_G and W_D represents the length of the graphene sample and width of the amorphous strip and A is the area of cross section for the heat flow ($A = W_G \times t$, where t is the thickness of the graphene sheet).

3.3 Results and discussions

The experimental results obtained from our collaborators are shown in Fig. 3.2. Fig. 3.2(a) shows the extracted average thermal conductivity of the graphene grains and GB regions for three tested devices having misorientation angles of 3°, 8° and 21°. The thermal conductivity of single crystalline graphene at room temperature is extracted to be 836 $\pm$ 126 $Wm^{-1}K^{-1}$. The figure reveals that an individual grain boundary can significantly reduce thermal conductivity in graphene structures, and the effect becomes more pronounced as the misorientation angle of the merged grains increases. In Fig. 3.2(b), the total thermal resistance from these three devices were calculated as— $R = L/(KWt)$ where L, W, and t are the length (5 μm), width (11.5 μm), and thickness (0.335 nm) of the graphene channel, and K is the average thermal conductivity values from Fig. 3.2(a). In Fig. 3.2(c), the conductance of the GB region is calculated as $G_{GB} = R_{GB}^{-1}$, where $R_{GB} = R_{GB-Region}(3°, 8°$ or $21°) - R_G$ (resistance of the graphene grains without GB).

In order to explain the order of magnitude difference between our experimental results and previous predictions [62], we used extensive theoretical modeling to elucidate

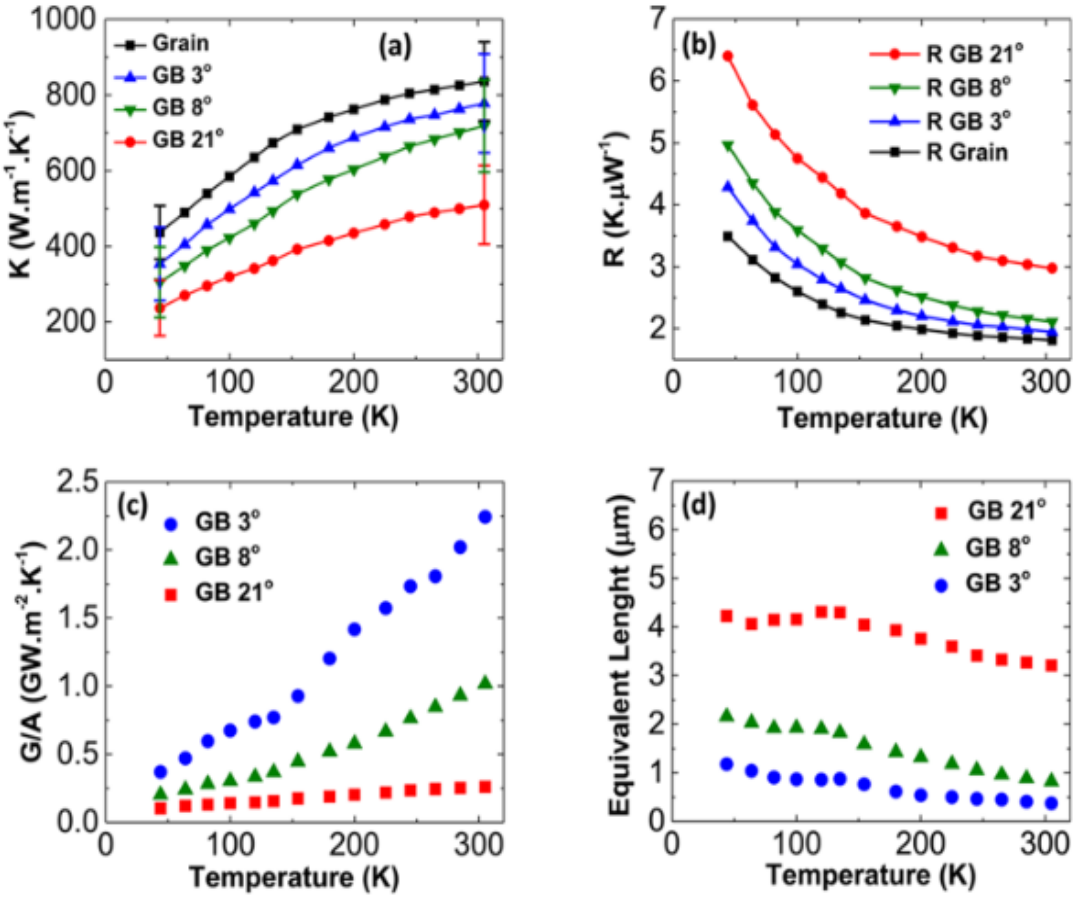

Figure 3.2. **(a)** Temperature-dependent extracted thermal conductivity of the single crystalline graphene and the GB region with different mismatch angles (3°, 8° and 21°). The error bars represent the overall uncertainty of the measurements. **(b)** Thermal resistance of the GB regions and the single-crystalline graphene grains. **(c)** The thermal conductance per unit area (G/A) of the different GBs. **(d)** The additional thermal resistance caused by an individual GB is shown as an equivalent extra length of the single grain with similar width [67].

the different phonon modes and their scattering mechanisms involved in thermal transport across the graphene GBs. Fig. 3.3(a) illustrates the variation of thermal conductivity with temperature for various grain mismatch angle, including the one with no grain mismatch angle, which basically represents perfect grain boundary. The misalignment in the boundaries of adjacent grains can be thought of as two single-crystalline grains are stitched to each other with a patch of disordered graphene. For low angle of grain mismatch, this disordered patch is so narrow that it can be approximated as line defect (LD) with some rms value of edge roughness depending on the angle of misalignment. For higher angles, this disordered patch is wide enough to add a considerable amount of additional resistance to the flow of heat so as to reduce thermal conductivity by a substantial amount. To sum up, the effect on thermal conductivity due to grain mismatch angle can be modeled as two separate phenomena first is the resistance due to scattering of phonons from the rough boundaries (edge roughness scattering) and second is the resistance due to additional patch of disordered graphene for large angle mismatch. The total thermal conductivity has been calculated as $K_{GB-Region} = W_G/(R_{GB-Region}A)$, where $R_{GB-Region}$ is the total resistance due to graphene with GB and amorphous patch and is given by $R_{GB-Region} = [(W_G - W_D)/(AK_G)] + [W_D/(AK_{min})]$. Here, W_G denotes the width of the graphene between heater and sensor ($5\mu m$), W_D is the width of the disordered region at the GB, and K_G denotes thermal conductivity of graphene without any GBs. K_{min} is the thermal conductivity of the disordered region calculated from Cahill′s minimum thermal conductivity model. Fig. 3.3(c) shows the effective G/A through a GB as a function of temperature. The G is calculated as the reciprocal of the resistance arising due to GB alone (R_{GB}) as ($G = 1/R_{GB}$), where $R_{GB} = [W_G/(AK_{GB-Region})] - [W_G/(AK_G)]$. It can be seen that the boundary conductance (G/A) results obtained from the solution of pBTE are in excellent agreement with the experimental data.

The effect of GB on the thermal conductivity due to different rms roughness (Δ) and the effect of disordered region due to its varying width (W_D) are complementary to each

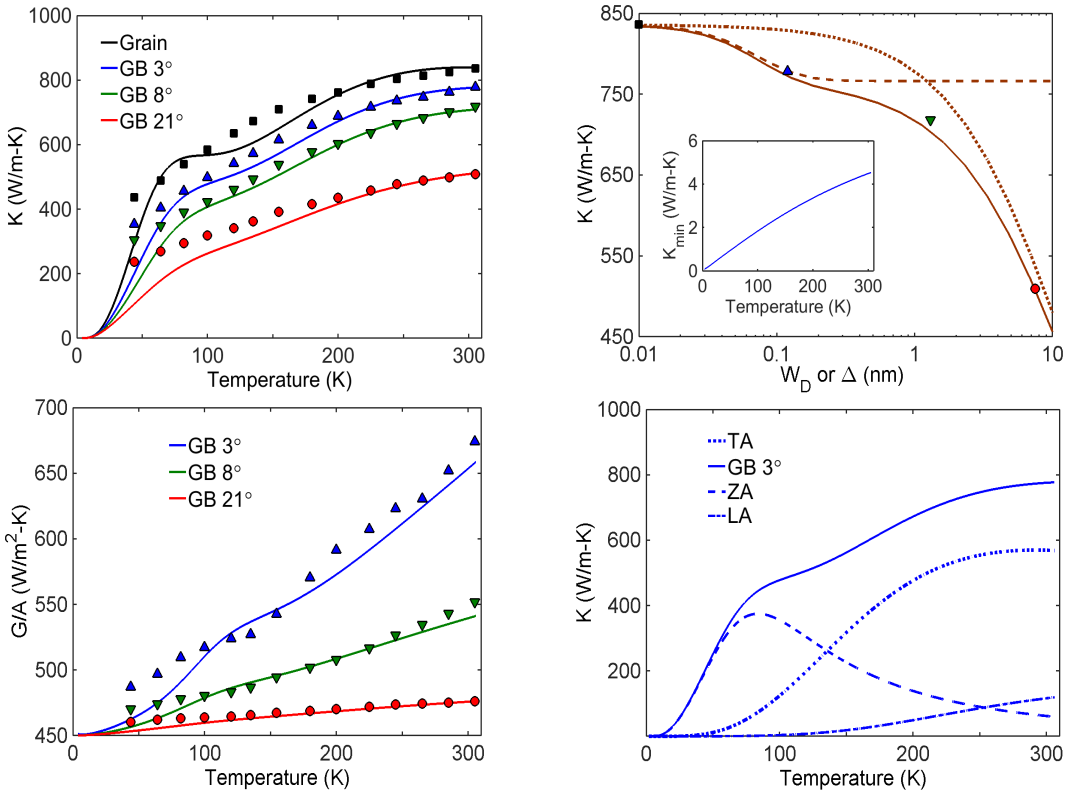

Figure 3.3. **(a)** Thermal conductivity vs temperature calculated from the phonon Boltzmann transport model. The symbols in **(a)** and **(c)** represent experimental data from Fig. 3.2(a) and (c), while solid curves represent simulation results. Panel b shows thermal conductivity at room temperature vs the grain boundary roughness Δ and the width of the disordered boundary region W_D. Solid curve shows total thermal conductivity vs W_D keeping Δ=0. Symbols represent experimental data at 300 K. The agreement with the experimental data is achieved by including a narrow strip of disordered graphene, whose conductivity is calculated from Cahill′s minimum thermal conductivity model, as explained in the text, and plotted in the inset of **(b)**. **(c)** Thermal conductance of the grain boundary vs temperature. The agreement in **(a)** and **(c)** is achieved using the following values for grain boundary roughness (Δ) and the width of the disordred region at GB (W_D): (1) without grain boundary: Δ=0 nm, W_D=0 nm; (2) 3° mismatch:Δ=0.12 nm, W_D=0.12 nm; (3) 8° mismatch: Δ=1.3 nm, W_D=1.3 nm; (4) 21° mismatch: Δ=7.5nm, W_D=7.5 nm. **(d)** Solid line shows thermal conductivity vs temperature for 3° grain mismatch angle, while dash, dash-dot, and dotted lines show its branch-wise components (ZA, TA, LA), respectively, with ZA carrying most heat at low temperatures, and in-plane modes (TA and LA) dominating at room temperature and above.

other because the effect of roughness saturates after Δ=0.25 nm. Fig. 3.3(b) shows that, for low values of Δ and W_D, the total thermal conductivity (solid curve) follows the thermal conductivity curve due to GB scattering alone (dashed curve) and, for higher values of Δ and W_D, follows the thermal conductivity curve due to the width of disordered strip alone (dotted curve). Hence, for small values of Δ and W_D (up to 0.25 nm), thermal conductivity is largely dominated by the GB scattering alone with negligible effect from the narrow disordered strip, in agreement with the experimental data for low mismatch angle. For higher values of Δ and W_D (beyond 0.25 nm), GB scattering becomes completely diffuse (p=0) and the effect of boundary roughness saturates. There is a natural crossover occurring at 1 nm, beyond which the total thermal conductivity is dominated by the additional resistance of the disordered region. This is in good agreement with the experimental data for large angle mismatch. Using the explained methodology, the experimental data for thermal conductance of the GB is well-reproduced for the entire temperature range (Fig. 3.3(c)). The individual contribution to thermal conductivity from each of the branches are shown in Fig. 3.3(d), with the out-of-plane acoustic (ZA) branch contributing at low temperatures, and in-plane (LA and TA) dominating above 150 K.

3.4 Conclusion

We observed that the thermal resistance at highly misoriented GBs can be remarkably higher than previous theoretical predictions owing to the larger disorder found in the atomic structure of GBs in CVD grown graphene. BTE calculations indicate that a bimodal scattering mechanism governs the phonon transport through the GBs: for small mismatch angles, thermal resistance of GB can be captured through phonon scattering from GB roughness, while for higher mismatch angles, the GB roughness effect is saturated. The lower thermal conductivity at higher mismatch angles can be explained through the presence of a narrow strip of disordered graphene at the GB. For the highest mismatch angle of 21°, we calculate the width of the disordered region to be 7.5 nm based on the minimum thermal conductivity

model. For intermediately misoriented GBs, thermal conductivity is affected by a complex interplay between the magnitude of grain boundary roughness and amount of disorder in the disordered patch. Our results show a direct correlation between GB thermal resistance and grain mismatch angles.

CHAPTER 4

EFFECT OF GRAIN BOUNDARIES IN TWO-DIMENSIONAL LATERAL GRAPHENE-CONTACTED MOS_2 HETEROSTRUCTURES

4.1 Introduction

In recent years, there have been a growing research interest in creating transistors out of high quality 2D heterojunctions, owing to their excellent electronic and thermal transport properties as well as compactness. Such devices have the potential to form the backbone of next generation electronic/optoelectronic industries. Besides graphene, transition metal dichalcogenides (TMDs) are a new family of two-dimensional materials, which are showing a future prospect for developing systems with reduced dimensionality. Molybdenum disulfide (MoS_2), being one of the most popular member of this group has shown interesting semiconducting properties, which makes it a promising candidate for digital electronic circuitry applications. However, MoS_2 has been reported to form Schottky contacts with most of the commonly used metals due to Fermi-level pinning phenomenon [8]; as a result it imposes large contact resistance on the extrinsic performances of these MoS_2-based devices [21]. Moreover, such metal-contacted devices do not have enough mechanical bendability to be used in flexible electronic applications. Therefore, there has been a growing interest in making transistors out of two flexible monolayer sheets and recent studies on 2-D transistors based on out-of-plane graphene contacted MoS_2 have been reported with improved performance as compared to the metal-contacted semiconductor transistors [70, 42, 69, 20, 71]. However, it has been found that the contact area in such vertical heterostructures is in the order of few micrometer, possibly to preserve the device mobil-

ity. This can seriously limit the count of transistors per chip for future high performance integrated electronics.

In this work, our collaborators fabricated nearly-perfect lateral MoS_2/Gr heterojunctions as shown in Fig. 4.1. The difference in the work functions and electron affinity of graphene and MoS_2 would lead to band-bending at the interface, which varies with the applied gate voltages; thus making it imperative to study the effect of grain boundaries on electron transport in such structures. We carried out numerical simulation in order to gain a comprehensive insight of the electric transport at the MoS_2/Gr grain boundaries for different gate voltages in bottom-gated lateral graphene-contacted MoS_2 heterojunctions. A new theoretical model based on energy band rearrangement has been developed to describe the electric transport behavior across the MoS_2/Gr grain boundary. The boundary resistance is modeled using a combination of first principles band structure calculations, followed by calculation of the transmission coefficient and grain boundary conductance in the Landauer formalism. We report that the grain boundary resistance decreases at higher gate voltages, which is also consistent with the Kelvin probe force microscopy (KPFM) results. We attribute such behavior to the improved band alignment and electron transmission between the two materials culminating in a negligibly small grain boundary contribution to the total resistance and results in ohmic behavior.

4.2 Theoretical modeling

To shed light on the origin of the improved electrical performance of the graphene-contacted MoS_2 devices, the individual electronic band structures of graphene and MoS_2 was calculated using first-principle Density Functional Theory as implemented within the open-source distribution Quantum-Espresso [26]. The total resistance (R_{tot}) of the whole device between source and drain is comprised of the series resistances from the graphene grains (R_{grap}, forming source and drain), resistance of MoS_2 grain (R_{MoS_2}), constituting the channel) and resistances from the grain boundaries (R_{GB}) formed at the interface

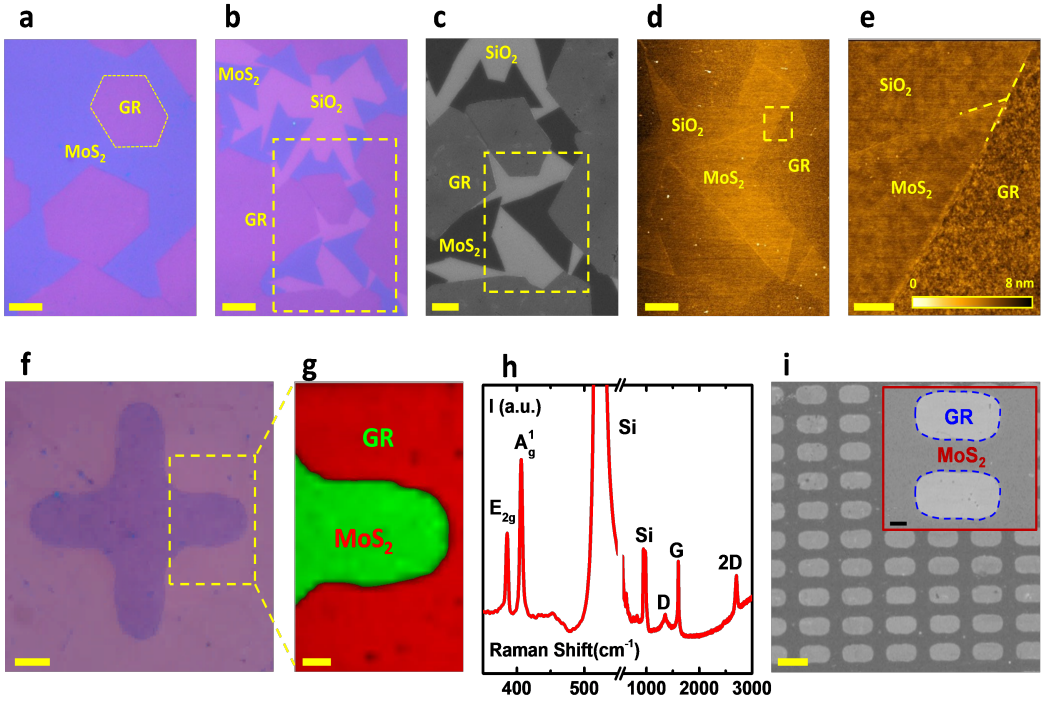

Figure 4.1. Microscopy and characterization of the MoS_2/Gr in-plane heterostructure. Optical image of **(a)** the fully covered MoS_2 film **(b)** partially covered MoS_2 flakes next to the partially covered graphene flakes (scale bars 10 m). **(c)** SEM image of the MoS_2/Gr in-plane heterostructure from the selected area in **(b)** (scale bar 5 m). **(d)** AFM image from the selected area of **(c)** (scale bar 5 m). **(e)** Higher magnification AFM image of the selected area in **(d)**, showing the boundary between MoS_2 and graphene (scale bar 300 nm). **(f)** Optical image of a cross-shape patterned graphene film which is filled with MoS_2 in a second CVD growth (scale bar 5 m). **(g)** Raman mapping of a selected area shown in (f) (scale bar is 2 m). **(h)** Representative Raman point spectra from the MoS_2/Gr boundary area. (i) SEM image of a large scale MoS_2/Gr in-plane heterostructure (scale bar 10 m) the inset magnifies the same image (Scale bar in inset 2 m) [9].

between graphene and MoS_2. We calculate the series grain resistances of graphene and MoS_2 sections from the general expression $R_{2D} = \rho L/W$, where ρ is the resistivity of the material (sheet resistance in this case) and L/W is the aspect ratio of the sample. The conductivity ($\sigma = 1/\rho$) of graphene and MoS_2 grain is calculated from $\sigma = qn\mu$, where n is the carrier concentration, μ is the carrier mobility.

4.2.1 Mobility calculation in MoS_2

The carrier mobility in graphene, which depends on its carrier concentration, is taken from the work by Dorgan et al. [23]. In addition to intrinsic phonon-limited carrier mobility in MoS_2 ($\mu_{ph} \sim 410\ cm^2V^{-1}s^{-1}$ [32]), the mobility is also influenced by factors like charged impurities, surface optical (SO) phonons and other short range scattering mechanisms. However, it has been reported that the electron mobility in MoS_2 is largely affected by the charged-impurity (CI) scattering [72, 73, 45]. An empirical expression for CI-limited mobility for MoS_2 has been adopted and modified from the work by Ma and Jena [45] and is given as: $\mu_{CI} \approx 45/(n_{imp}(10^{11}(cm)^{-2}))(A(\epsilon) + ((C_{oxide}V_g + n_{imp})/(10^{13}(cm^{-2}))^{1.2})$, where $A(\epsilon)$=0.036 is a fitting constant depending on the dielectric constant of SiO_2 (oxide layer), C_{oxide} is the capacitance per unit area of the gate oxide and n_{imp} is the charged-impurity density. The impurity density equals sheet charge density ($n_C = C_{oxide}V_g + n_{imp}$) at zero gate voltage. We use an impurity concentration of $5.5 \times 10^{11}(cm^{-2})$, which is found by fitting the finite resistance at zero gate voltage obtained from experimentally measured $I_d - V_{DS}$ data. In the presence of multiple scattering mechanisms, the mobility of the free carriers can be represented by Matthiessen's rule and is given as: $\mu_{MoS_2} = (\mu_{ph}^{-1} + \mu_{CI}^{-1} + \mu SR^{-1})^{-1}$, where μ_{SR} is the mobility due to short range effects [73].

4.2.2 Electronic bandstructure alignment between graphene and MoS_2

Due to the difference in work function and electron affinity of graphene and MoS_2, there will be band-bending at their interface. The electron affinity (an intrinsic property of a semiconductor) of MoS_2 (χ_{MoS_2}) and graphene (χ_{grap}) is 4.2 eV and 4.55 eV respectively;

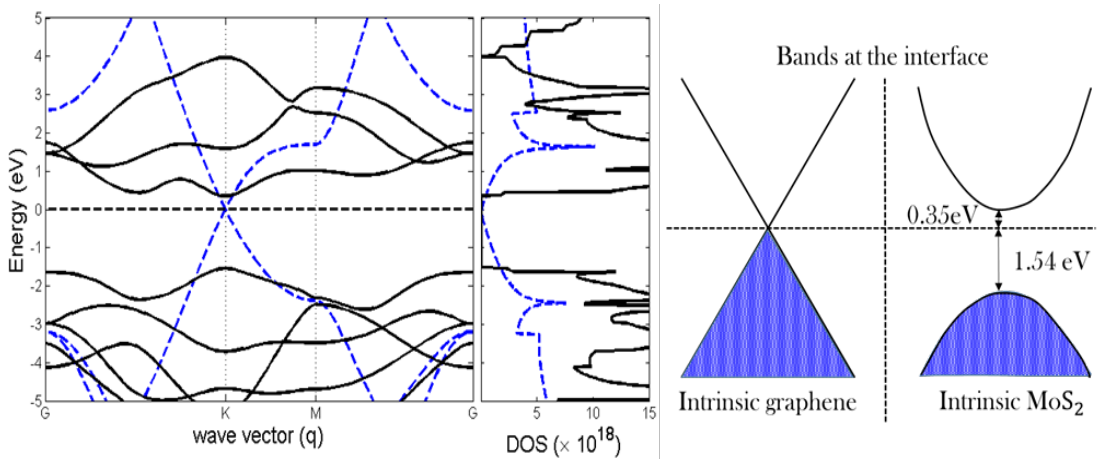

Figure 4.2. **(a)** Electronic band structure and **(b)** DOS of MoS_2 (solid black lines) and graphene (dashed blue lines), showing the band alignment at the interface. There is a 0.35 eV Schottky barrier at the interface **(c)**.

whereas the work function in a semiconductor, depends on the gate voltage, is given as: $\phi = \chi + E_c - E_F$, where E_c represents the bottom of the conduction band and E_F is the fermi energy level. The barrier height ϕ_B, when seen from graphene towards the MoS_2, can be calculated as: $\phi_B(V_g) = \phi_{grap}(V_g) - \chi_{MoS_2}$. And the amount of band-bending in MoS_2 at the interface is given by the difference in energies of the conduction band bottom at and away from the interface i.e. $\phi_{interface}(V_g) = \phi_{MoS_2}(V_g) - \chi_{MoS_2} - \phi_B(V_g)$. The electronic band structure alignment of graphene and MoS_2 at the interface has been shown in Fig. 4.2 and the band-bending is shown in Fig. 4.3.

4.2.3 Transmission coefficient and grain boundary resistance calculation

To calculate the grain boundary resistance, we develop a numerical model to calculate the transmission coefficient of electrons from the graphene to MoS_2. In our model, we include both the effect of the potential barrier at the interface and the mismatch in the electronic structures of the two materials by requiring both electron energy and the component of the wavevector parallel to the interface to be simultaneously conserved. This approach expands the method originally proposed by Yazyev and Louie [68] for electron transmission through graphene/graphene grain boundaries and allows us to calculate the dependence of

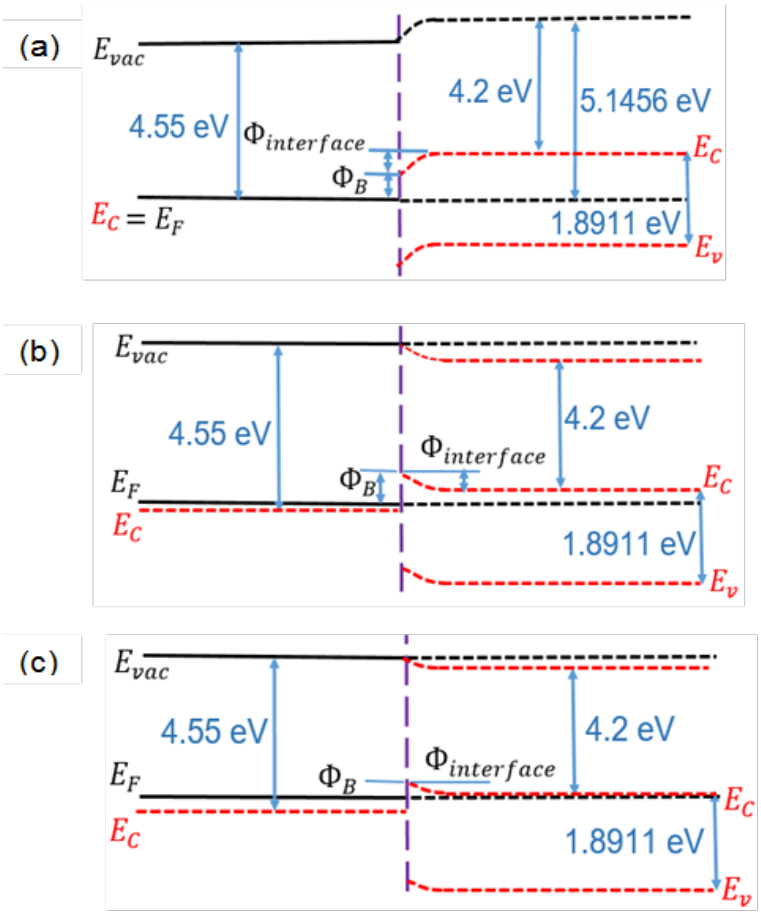

Figure 4.3. Band alignment between MoS_2 and graphene, showing the Schottky barrier at the interface and band bending in the MoS_2, indicating an n-type Ohmic contact for **(a)** intrinsic graphene and MoS_2 at V_g=0 V and a small barrier height for **(b)** extrinsic graphene and MoS_2 at V_g=0 V **(c)** at V_g=60 V.

GB resistance on the band alignment between the two domains. The momentum conservation principle requires that: (i) the magnitude of parallel component of the incident wave vector ($k_{i\|}$) be equal to the magnitude of parallel component of the transmitted wave vector ($k_{t\|}$), in their respective domains; and (ii) energy is conserved by finding a perpendicular component of the transmitted wave vector ($k_{t\perp}$) such that $E_1(k_i) = E_2(k_{t\|} + k_{t\perp})$ and $k_{t\perp}$ is within the 1st Brillouin zone of the respective domain. The transmission coefficient is then calculated using the perpendicular components of the incident ($k_{i\perp}$) and transmitted ($k_{t\perp}$) wave vectors using a general expression for wave transmission between two domains [16] given by $\tau_b(k_i) = (4k_{i\perp}k_{t\perp})/\mid k_{i\perp} + k_{t\perp} \mid^2$, where b represents electron band. Finally, the energy-resolved transmission coefficient $\Gamma_b(E)$ is calculated by averaging the product of transmission coefficient $\tau_b(k)$ and electron group velocity $v_b(k)$ over the constant energy contour, described by $\delta(E - E_b(k))$, using the 2-dimensional version of the linear extrapolation approach described by Gilat and Raubenheimer [27] and then we calculate transport distribution function (TDF) as follows:

$$\Xi(E) = \sum_b = v_b(E)\Gamma_b(E)D_b(E) = \sum_b (1/4\pi^2) \int v_b(k)\tau_b(k)\delta(E - E_b(k))dk \quad (4.1)$$

The TDF is then used to numerically calculate the grain boundary conductance in a Landauer formalism and inverted to obtain the grain boundary resistance R_{GB}, calculated by inverting the grain boundary conductance which is obtained from an integral of the TDF over energy:

$$R_{GB}^{-1} = G_{GB} = e^2/2 \int_{E_C}^{E_{max}} \Xi(E)(-\partial f(E - E_F, T)/\partial E)dE \quad (4.2)$$

where E_C is the bottom of the conduction band and E_{max} is the highest electron energy in the first four conduction bands.

4.3 Results

On applying gate voltage, but before any source-drain bias is applied, the Fermi levels in both graphene and MoS_2 away from the interface shift relative to their position at zero gate voltage in response to the induced charge in the 2-dimensional layers, as shown in Fig. 4.4(a). Consequently, the energy bands on both sides of interface rearrange themselves to maintain the equilibrium condition. However, the shift in the bands on the two sides is not identical because the two materials have different densities of states, leading to an increase in band bending in the MoS_2 with increasing gate bias. The transmission coefficient of electrons across the grain boundary, however, depends on the alignment of energy bands at the interface between graphene on one side and MoS_2 on the other. For example, states near the Fermi level in graphene cannot typically be transmitted because there are no available states at the same energy in MoS_2 as energies near the Fermi level fall inside the bandgap. Increasing the gate bias raises the sheet charge in both graphene and MoS_2; in response, the Schottky barrier between graphene and the conduction band in MoS_2 decreases with gate bias (Fig. 4.4(a)), in agreement with KPFM measurements.

As a result of band rearrangement and barrier lowering, the transmission Γ(E) also shows a dependence on gate voltage. It can be seen in Fig. 4.4(b) that with increasing gate voltage, the transmission coefficient Γ(E) shifts towards the left, resulting in larger overlap between Γ(E) and the so-called Fermi window (-df/dE) which is centered at the Fermi level. This gives rise to gate-voltage-dependent grain boundary resistance, as shown in Fig. 4.4(c), paralleling the reduction in the resistance of MoS_2 grain which arises from both the increase in sheet charge and mobility (conductance calculation described further in Methods). Overall, the contribution of the grain boundary resistance to the total resistance of the combined MoS_2+GB+graphene system decreases with gate bias, starting at around 25% of the total in the intrinsic (zero gate) case, and rapidly dropping below 1% at gate voltage of 60 V, as shown in the inset to Fig. 4.4(c), closely paralleling the KPFM measurements of the grain boundary contribution. The agreement between measured and

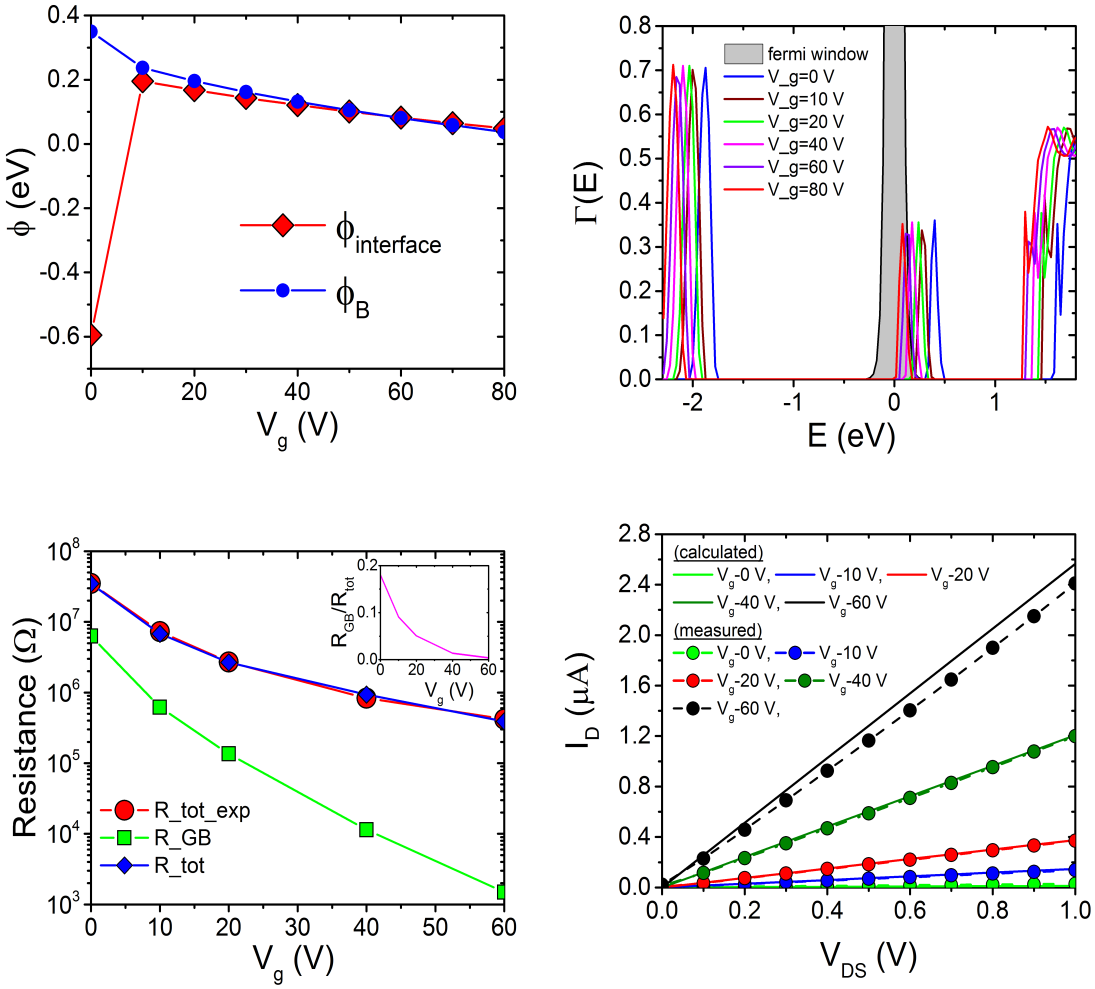

Figure 4.4. **(a)** shows the variation in grain boundary Schottky potential barrier height from graphene to MoS_2 (ϕ_B) and from MoS_2 to graphene ($\phi_{interface}$) with gate voltage (V_g). **(b)** resulting shift in transmission coefficient with gate voltage, such that with the increasing V_g a larger part of Γ(E) overlaps with the Fermi window (shown by the grey area in the plot) resulting in increased conductance. **(c)** grain boundary resistance (R_{GB}) and the total resistance (R_{tot}) both measured (red line with red markers) and calculated (black line with black markers) against gate voltage. The inset shows the percentage contribution of grain boundary resistance (R_{GB}) towards the total resistance (R_{tot}) of the device at different gate voltages, in good agreement with KPFM measurements. **(d)** drain current (I_D) vs. drain-source voltage (V_{DS}) calculated both experimentally and by numerical simulation showing good agreement between numerical and experimental results.

calculated total resistances, mathematically written as $R_{tot} = 2R_{grap} + R_{MoS_2} + 2R_{GB}$ and shown in Fig. 4.4(d), indicates that the measured resistances are well reproduced by the model and that at most non-zero gate biases, the grain boundary contributes very little to the overall resistance, leading to ohmic behavior.

4.4 Conclusion

In this work, we calculated I-V characteristics in 2D transistors with graphene and MoS_2 lateral heterojunctions, which exhibit improved electrical performance in comparison to metal-MoS_2 devices and similar electrical performance to that of vertical graphene-MoS_2 heterostructures with large contact area. However, lateral heterostructures have atomically narrow contact area. This makes in-plane MoS_2/Gr heterostructures promising for large scale production of electronic and logic circuits from all-2D materials for next generation device applications. The numerical calculations reveal that both the barrier at the interface as well as the resulting grain boundary resistance decrease as sheet charge is increased in response to the external gate voltage. At gate voltages above 60 V, the interface contributes less than 1 % of the MoS_2 region despite the appreciable electron mobility in the MoS_2, resulting in the observed linear (ohmic) behavior. This work uses a simple, novel theoretical model to calculate electronic grain boundary resistance across interfaces formed between different materials, thereby would help us to gain more insight about electronic conduction across complex grain boundaries. This work assumes no grain angle misorientation between materials across the interface and resulting into small grain boundary resistance in comparison to the total resistance of the device. However, it would be very interesting to investigate the effect of grain angle mismatch on grain boundary resistance.

CHAPTER 5

IMPACT OF MISMATCH ANGLES ON ELECTRONIC GRAIN BOUNDARY/INTERFACE RESISTANCE IN LATERAL TWO-DIMENSIONAL HETEROSTRUCTURE

5.1 Introduction

Graphene, a monolayer of sp^2 hybridized carbon atoms arranged in a honeycomb lattice structure, has a unique electronic band structure because of which it exhibits numerous interesting properties including quasi-ballistic electrical transport up to several microns of length even at room temperature. Besides graphene, transition metal dichalcogenides (TMDCs) are another class of two-dimensional materials which have attracted intense research interests in recent years. The potential applications of graphene and TMDCs have motivated mass scale production of large-area films. Among the most popular methods, chemical-vapor deposition (CVD) on transition metal substrates is relatively cheap and extensively used to grow high quality large two-dimensional sheets. However, CVD-grown films are typically found to be polycrystalline in nature, consisting of many single crystalline grains each with random crystal orientation and separated by grain boundaries (GBs). Many studies have reported that grain boundaries deteriorate both electronic and thermal properties.

The effect of grain boundary roughness on electronic transport in graphene and MoS_2 is negligible because the dominant electron modes are located around K-valleys and have relatively short wavelength; as a consequence, the rough GBs are expected to behave rather coherently. However, the difference in orientation between adjacent grains play a significant role in electron transport across an interface formed between both similar (homojunction) and dissimilar (heterojunction) materials. In spite of numerous studies of the

effect of misorientation angle on the electronic transport across graphene grain boundaries [29, 19], and very few of MoS_2 GBs [43] (and to the best of our knowledge, none yet for graphene-MoS_2 lateral interfaces), a complete picture of the impact of mismatch angle on interface resistance requires further investigation. Huang et al. [29] showed a wide range of distribution of misorientation angles between adjacent grains in polycrystalline single-layer graphene sheet with a preferential low angle growth of about 7°. The GB resistance across such GBs was found to be about 60 $\Omega\ \mu m$ as compared to a sheet resistance of 700 $\Omega/\square$ for the entire device of size 250 nm. Thus, they show that the GB resistance is about one-third of the grain resistance with grain size of 250 nm and thereby, concluded that graphene GBs don't play a significant role in determining resistance of polycrystalline graphene sheets. Clark et al. [19], in 2013, found GB resistance to be varying between 40-140 $\Omega\ \mu m$ for misorientation angles ranging from 9° to 21°. Recent studies have shown graphene GB resistance to vary from few $\Omega\ \mu m$ to several thousands of $\Omega\ \mu m$ suggesting a strong dependence of grain boundary resistance on mismatch angles. Ly et al. [43] showed that MoS_2 sheets exhibit very poor electrical transport properties (mobilities below 70 $cm^2V^{-1}s^{-1}$) for all the devices with different misorientation angles. However, they did not conduct any four-probe measurement to calculate the GB resistance separately. Therefore, a further investigation about the fundamentals behind the effect of GBs and interfaces in homojunctions and heterojunctions is imperative.

In the previous chapter, we discussed about the resistance across a heterojunction formed between graphene and MoS_2 but for only perfectly-matched grains. In this work, we investigate electron transport across GBs in graphene, MoS_2, and graphene-MoS_2 lateral interfaces. To study the impact of misorientation angle, we have developed a numerical model based on first-principles electronic structure and an extension of the approach originally proposed by Yazyev and Louie [68] to calculate the transmission coefficient of electrons across an interface based on elastic theory by simultaneously conserving both electron energy and the component of the wavevector parallel to the interface. The orientation of the

grains with respect to the GB/interface is defined by two angles — θ_L and θ_R. θ_L being the angle of rotation between the grain on the left side of the interface with respect to the interface and θ_R is the angle of rotation of the right grain with respect to the interface as shown in Fig. 5.1. According to our convention, θ_L is taken to be positive for anticlockwise rotation of the left grain, whereas, θ_R is positive for clockwise rotation of the right grain. We define misorientation angle (θ) as $\theta = \theta_L + \theta_R$.

As discussed in Chapter 3, when the misorientation angle (θ) between two grains is small then the GB/interface mainly comprises of edge dislocations and the atomic structure of the grain boundary itself doesn't play much role in determining grain boundary resistance. However, for larger values of θ the dislocations become so densely packed that it is no longer fair to treat them as mere dislocations rather it forms a disordered patch at the interface. Owing to the small wavelength of electrons, in general, the disordered (amorphous) patch scatters electron diffusively; consequently, GB resistance is not affected significantly due to the presence of amorphous patch in case of large misorientation angles. However, in this study we ignore the effect of the atomic structure of the grain boundary, even in the case of large mismatch angles.

5.2 Theoretical approach

In our numerical model we calculate the electronic bandstructure for bulk graphene and MoS_2 from first principles. The bands are aligned at the interface using electron affinity model. The effect of grain boundary/interface is incorporated using boundary conditions based on elastic theory. From translational symmetry, elastic transmission requires simultaneous conservation of energy of the incident electron as well as conservation of its momentum parallel to the interface. Here we assume the interfaces are free from trapped and surface impurities; consequently the bands are assumed to be well-aligned across the interface with same materials on either side. However, due to the difference in work function (ϕ) and electron affinity (χ) of graphene and MoS_2, the bands bend at the graphene-MoS_2

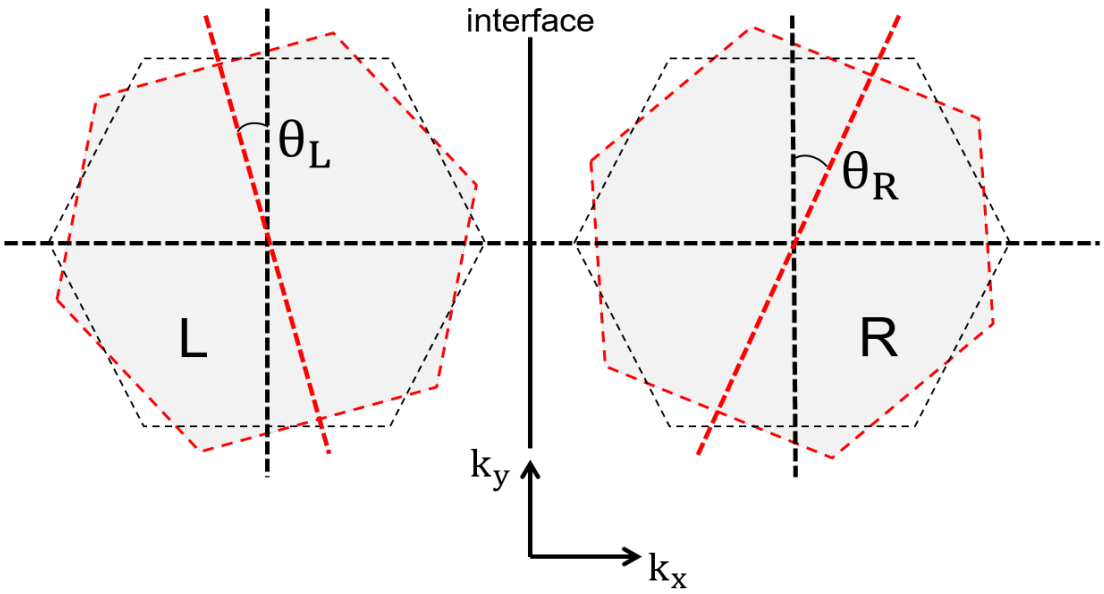

Figure 5.1. shows orientation of the grains with respect to the interface. The black hexagons represent the orientation of the brillouin zones for perfectly matched condition ($\theta_L = \theta_R = 0°$). θ_L is the angle of rotation, measured in anticlockwise direction, between the rotated left grain (red) and the one for perfectly-matched condition (black) and θ_R is the angle of rotation, measured in clockwise direction, between the rotated right grain and the grain for perfectly-matched condition.

interface and a potential barrier is formed at the interface. The barrier height is calculated as $\phi_B(V_G) = \phi_{graphene}(V_G) - \chi_{MoS_2}$ and the amount of band-bending on MoS_2 side is given by $\phi_{interface}(V_G) = \phi_{MoS_2}(V_G) - \chi_{MoS_2} - \phi_B(V_G)$. On aligning the band structures, we calculate mode-dependent transmission coefficient ($\tau_b(\vec{k})$) for each branch b. For including the effect of misorientation angle, the wavevectors in the first brillouin zone are rotated by θ_L for the left grain and θ_R for the grain on the right hand side of the interface and then mode-dependent transmission coefficient is calculated. Transmission is computed on the basis of thermionic emission and tunneling is neglected in this current model. As mentioned in chapter 4, transmission coefficient is given by this expression — $\tau_b(k_i) =\mid 4k_{i\perp}k_{t\perp} \mid / \mid k_{i\perp} + k_{t\perp} \mid^2$, where k_i is the incident wavevector, k_t is the wavevector of the transmitted wave and the subscript $\perp$ stands for the perpendicular component of wvaevector. The grain boundary conductance is calculated using Landauer formalism as given in eqn. 4.2 in Chapter 4.

5.3 Results and discussion

Before discussing about the impact of mismatch angle between two grains on grain boundary resistance (R_{GB}), we calculated ballistic resistance in graphene-graphene (Gr-Gr) interface and compared it with analytically calculated values. We define ballistic resistance as the resistance between two perfectly-matched grains i.e. when misorientation angle is 0°. Let us first discuss about how to calculate ballistic resistance of graphene-graphene interface.

5.3.1 Ballistic resistance of graphene-graphene interface

The quantum conductance is the maximum conductance that can be obtained from a perfect 1-D conductor and maximum conductance is achieved when transmission coefficient is 1 for all the modes. Thus the quantum conductance is called ballistic resistance for 1-D conductor and is given by the expression — $G_{ball,1D} = 2q^2/h$, where q is the charge of

the carrier and h is the Planck's constant. Using the expression of ballistic conductance for 1-D conductor, the ballistic conductance for a two-dimensional conductor is given by—

$$G_{ball,2D} = G_{ball,1D} \times M_{2D}(E_F) \tag{5.1}$$

where $M_{2D}(E_F)$ is the number of 1-D channels available for conduction in width W for a two-dimensional ribbon and from now onwards will be referred to as channel number. The channel number at any energy (E) for a given width of the ribbon is calculated as [47]

$$M(E) = W\frac{h}{4}<v_x(E)>D_{2D}(E) \tag{5.2}$$

where $<v_x(E)>$ is calculated by 2-D averaging of velocity of all the modes, $<v_x(E)> = \frac{2}{\pi}v_F$. v_F is the Fermi velocity ($\approx 10^6\ ms^{-1}$), which is calculated as the slope of the dispersion (E-k relationship) around Dirac point. $D_{2D}(E)$ is the 2-D density of states.

5.3.1.1 Calculation of density of states, carrier density, and channel number in graphene

The dispersion of graphene around Dirac point is approximated by the relation— $E(\vec{k}) = \hbar v_F \mid \vec{k} \mid$, where $\hbar$ is the reduced Planck's constant. The general expression for calculating 2-D density of states is

$$D_{2D}(\vec{k}) = \frac{1}{(2\pi)^2}\frac{2\pi \mid k \mid}{\nabla_k E(\vec{k})}g_s g_v \tag{5.3}$$

where g_s and g_v are constants related to the spin of electron and valley degeneracy respectively. For graphene g_v=2 and g_s=2 for electrons. $\nabla_k E(\vec{k})$ is the gradient of energy dispersion with respect to the wavevector and around Dirac point it can be approximated by $\hbar v_F$. Thus for graphene,

$$D_{2D}(E) = \frac{2}{\pi\hbar^2 v_F^2} \mid E \mid \tag{5.4}$$

In general, 2-D carrier density is given as

$$n_{2D}(E_F) = \int_0^\infty f_0(E)D_{2D}(E)dE \tag{5.5}$$

where $f_0(E)$ is the Fermi-Dirac distribution function and can be written as $f_0(E) = [1 + exp(\frac{E-E_F}{K_BT})]^{-1}$. As graphene is degenerate, so eqn. 5.5 can be approximated by—

$$n_{2D}(E_F) = \int_0^{E_F} D_{2D}(E)dE = \int_0^{E_F} \frac{2}{\pi\hbar^2 v_F^2} EdE = \frac{E_F^2}{\pi\hbar^2 v_F^2} \tag{5.6}$$

Using the expressions for density of states and 2D-averaged velocity, channel number in eqn. 5.2 for graphene can be written as—

$$M_{2D}(E_F) = \frac{2}{\pi}\frac{E_F}{\hbar v_F} W \tag{5.7}$$

Replacing the expression for channel number obtained from eqn. 5.7 in eqn. 5.1, we can calculate ballistic conductance in graphene as

$$\frac{G_{ball,2D}}{W} = \frac{8q^2}{\hbar^2 v_F} E_F \tag{5.8}$$

From eqn. 5.6 and 5.8, ballistic conductance in graphene can be expressed in terms of carrier density as—

$$\frac{G_{ball,2D}}{W} = \frac{4q^2}{h}\sqrt{\frac{n_{2D}}{\pi}} \tag{5.9}$$

Thus the ballistic resistance (R_{ball}) in graphene, which is the reciprocal of $\frac{G_{ball,2D}}{W}$, is inversely proportional to the square root of carrier density. On using the values of the constants in eqn. 5.9 and intrinsic carrier density of $8 \times 10^{10}\ cm^{-2}$, the analytical value of R_{ball} in graphene is about 405 $\Omega\ \mu m$.

We compare analytically calculated values of ballistic resistance for different carrier densities with our numerically calculated values as shown in Fig. 5.2(b). At intrinsic carrier concentration ($n_0 = 8 \times 10^{10}\ cm^{-2}$), the numerically calculated ballistic resistance is 424 $\Omega\ \mu m$, which compares quite well with the analytical value of 405 $\Omega \mu m$. In Fig. 5.2(a) we can see that transmission coefficient [T(E)] is about 1 for all energies showing perfect

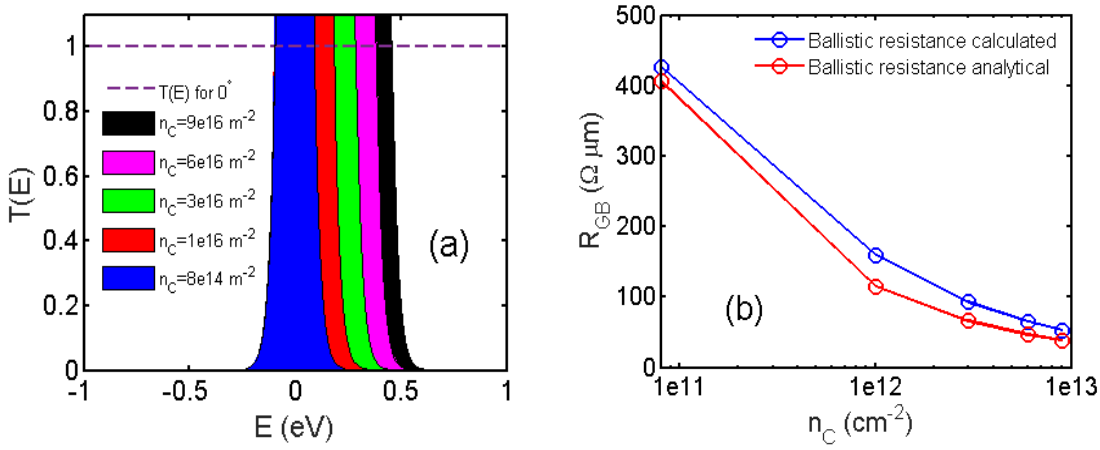

Figure 5.2. **(a)** shows perfect transmission for 0° mismatch angle between two graphene grains. The curves outlining the area in different colors represent Fermi window function ($-df/dE$), which is symmetric about E_F, for different carrier densities. **(b)** shows comparison between numerically and analytically calculated values of GB resistance (R_{GB}) with carrier density. R_{GB} is inversely proportional to the square root of the carrier density.

transmission for 0° mismatch (perfectly-matched grains). The curve encompassing the blue area in the figure is the Fermi window function, which is defined as the derivative of Fermi-Dirac distribution function w.r.t. energy, for intrinsic carrier density i.e. when Fermi level (E_F) is around Dirac point and the number of free electrons is equal to the number of free holes. Eqn. 4.2 shows that the grain boundary resistance is a function of transmission coefficient, Fermi window function, velocity (proportional to Fermi velocity in graphene, which is a constant) and density of states. When the carrier (electron) density increases the Fermi level goes inside the conduction band and as a result Fermi window function, which is symmetric about Fermi level, also shifts accordingly as shown in Fig. 5.2(a). The integral of the product of Fermi window, transmission coefficient and velocity w.r.t. energy is same for all carrier density but it is due to the 2-D density of states, which is independent of Fermi level, in the integral of grain boundary resistance that causes the difference in R_{GB} when plotted against carrier density as shown in Fig. 5.2(b).

In two dimensional materials depending on the orientation of each grain with respect to the grain boundary and orientation of the grains with respect to each other, grain boundaries

(GB) can be of different types. Here we have discussed about two particular types of GBs — the first is when both the grains are rotated by equal angles w.r.t. the GB but one in clockwise and the other in anticlockwise direction (i.e. $\theta_L = \theta_R$) and the second is when both the grains are rotated by different angles w.r.t. the GB (i.e. $\theta_L \neq \theta_R$). In literature, the former type of grain boundaries are referred to as twin GBs and the latter as tilt GBs.

5.3.2 Electron transport across graphene grain boundaries

Fig. 5.3(a) and Fig. 5.3(b) show transmission coefficient [T(E)] and GB resistance (R_{GB}) respectively for various misorientation angles in twin GBs. We see in Fig. 5.3(a) that perfect transmission is obtained for all the modes at any given energy level. But with the increase in misorientation angle, some of the modes get reflected and remaining get transmitted, consequently resulting in the reduction of transmission coefficient, which varies between 0.8 and 0.5 for various mismatch angles. However, we note that even for large mismatch angles there is no transmission gap in the energy spectrum. Due to the misorienation angle between two grains, if there is a region around Dirac point ($\approx$ 0 eV in our case) in the energy spectrum where transmission coefficient is zero, we call it— transmission gap. Perfect transmission at 0° mismatch angle translates into ballistic resistance across graphene GBs as shown in Fig. 5.3(b) [same as the blue curve in Fig. 5.2(b)]. The reduction in transmission coefficient with increasing misorientation angle maps into increase in grain boundary resistance as can be seen in Fig. 5.3(b). When the carrier density increases the Fermi level goes into the conduction band and, consequently, Fermi window function $[-df/dE]$ also shifts towards higher energy level. As density of states in graphene is proportional to energy around Dirac point (from eqn:5.4), thus, the value of the integral in eqn. 4.2 increases. As a result of which we see a decrease in GB resistance with increasing carrier density in Fig. 5.3(b).

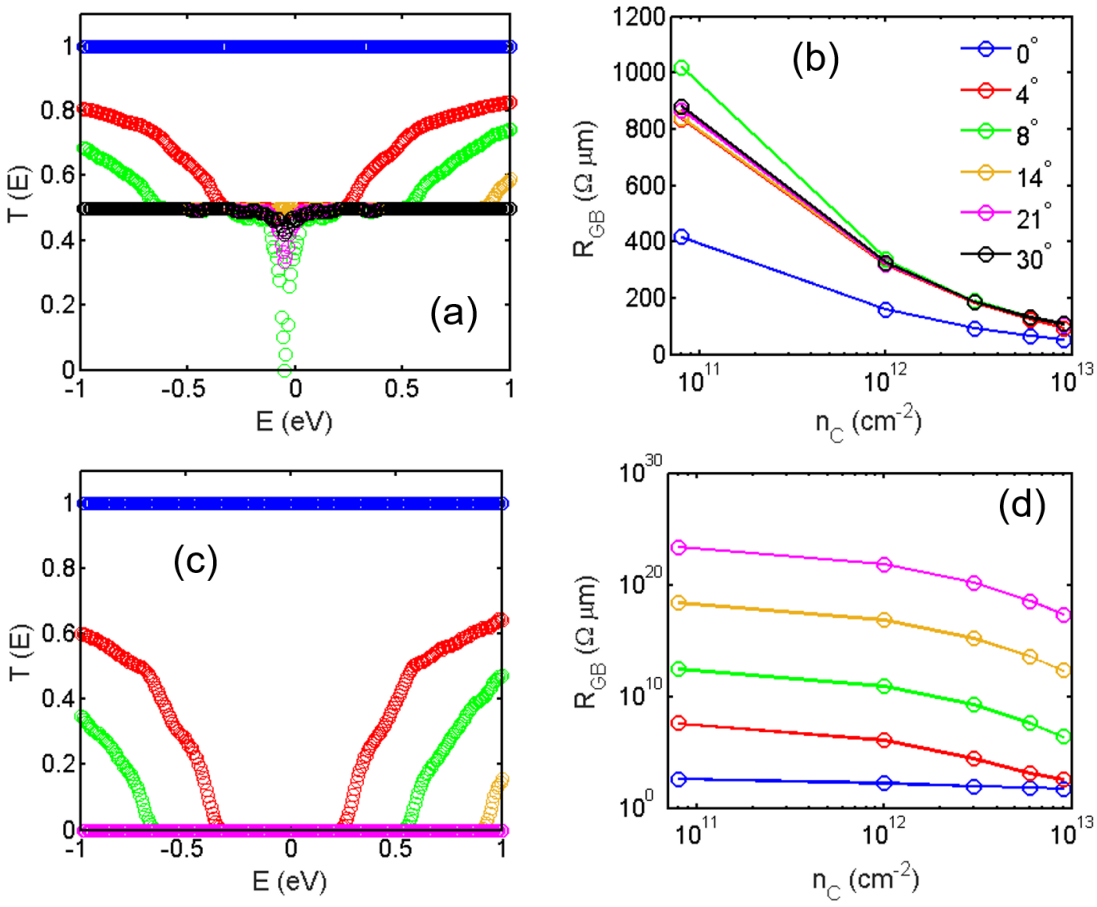

Figure 5.3. **(a)** shows transmission coefficient vs. energy for various misorientation angles across graphene twin grain boundaries. **(b)** shows the variation of grain boundary resistance with carrier density for the same mismatch angles as plotted in **(a)**. The curves for large mismatch angles— $14°$, $21°$ and $30°$ are overlapped on each other in both **(a)** and **(b)**. Transmission coefficient vs. energy and the resultant GB resistance vs. carrier density for different misorientation angles in graphene tilt GBs are plotted in **(c)** and **(d)** respectively. A transmission gap opens up for such tilt GBs.

Fig. 5.3(c) and Fig. 5.3(d) show transmission coefficient [T(E)] and grain boundary resistance respectively for various mismatch angles in tilt grain boundaries. Transmission coefficient shows a similar reduction with increasing mismatch angles as seen in Fig. 5.3(a), however, the reduction is more rapid than in the case of twin GBs. In such GBs, we also observe widening of the transmission gap with increasing misorientation angle. The transmission becomes zero for large misorientation angles i.e. beyond $10°$ mismatch. This transmission gap around Dirac point maps into large GB resistance for large angle tilt

GBs and also grain boundary resistance becomes less sensitive to the variation in carrier densities. In the literature, we find that the GB resistance across graphene GBs varies within a wide range— few $\Omega\mu m$ to 50000 $\Omega\mu m$. The reason for such wide variation in GB resistance can, thus, be explained clearly with the trends observed in 5.3(b) and 5.3(d) for twin and tilt GBs respectively.

5.3.3 Electron transport across MoS_2 grain boundaries

To study electronic resistance across MoS_2 GBs, we use the same set-up as used for graphene GBs in the previous section. The transmission coefficient as a function of energy is plotted in Fig. 5.4(a) for different misorientation angles in twin GBs. The blue curve shows transmission across an imaginary grain boundary (which corresponds to 0° mismatch). A perfect transmission is obtained for energies greater than about 0.94 eV and less than about -0.94 eV. Zero transmission at energies between -0.94 eV and 0.94 eV corresponds to the energy band gap of 1.88 eV in intrinsic MoS_2. We also observe a gradual reduction in transmission coefficient with increasing misorientation angles. A similar absence of transmission gap is found in MoS_2 twin GBs as was also observed in graphene twin GBs. Corresponding to the transmission coefficient for various misorientation angles, the boundary resistance across MoS_2 twin grain boundaries vs. carrier density is shown in Fig. 5.4(b). We note that the values of R_{GB} in MoS_2 twin GBs are almost double than the values of GB resistance in graphene twin boundaries for a carrier density of $1 \times 10^{12}\ cm^{-2}$ but for large values of carrier densities, i.e. 6×10^{12} and $9 \times 10^{12}\ cm^{-2}$, MoS_2 twin GBs have almost same resistance as graphene twin GBs.

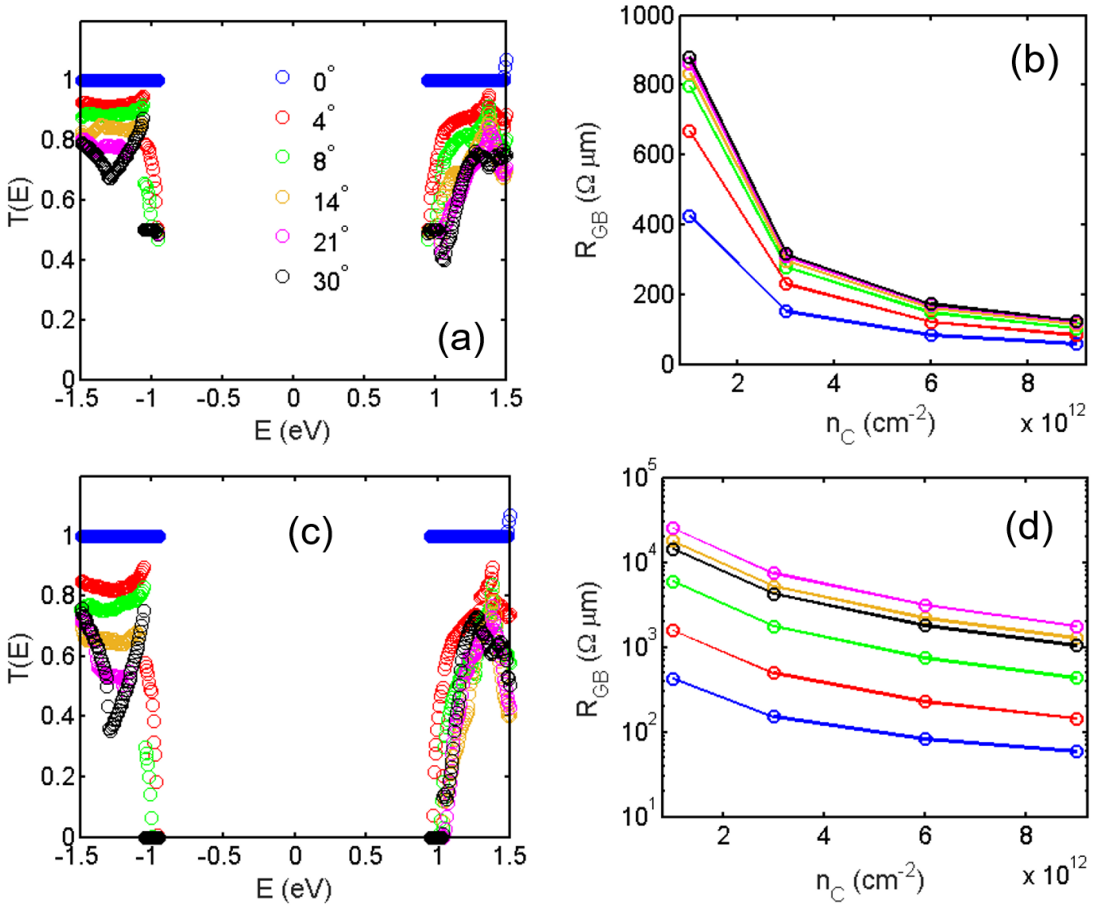

Figure 5.4. **(a)** shows transmission coefficient vs. energy for various misorientation angles across MoS_2 twin grain boundaries. **(b)** shows the variation of grain boundary resistance with carrier density for the same mismatch angles as plotted in **(a)**. Transmission coefficient vs. energy and the resultant GB resistance vs. carrier density for different misorientation angles in graphene tilt GBs are plotted in **(c)** and **(d)** respectively. Apart from intrinsic band gap, an additional transmission gap opens up for large tilt GBs.

Fig. 5.4(c) and Fig. 5.4(d) show transmission coefficient vs. energy and GB resistance vs. carrier density respectively for various misorientation angles in MoS_2 tilt GBs. It can be seen in Fig. 5.4(c) that transmission coefficient decreases with increasing msiorientation angle and the rate of reduction of transmission coefficient is rapid than what was observed in MoS_2 twin GBs. Like in tilt graphene GBs, a transmission gap is also observed in tilt MoS_2 GBs for large misorientation angles. The variation of GB resistance with misorientation angle is quite distinct in this case as compared to the variation of R_{GB} in graphene tilt

GBs. It is important to note that the resistance across MoS_2 GBs is much smaller than what we found in case of graphene GBs. Thus, misorientation of adjacent grains across grain boundaries can cause a significant reduction in electronic conductance in polycrystalline graphene; however, GBs in polycrystalline MoS_2 might not play much role in electron conduction.

5.3.4 Electron transport across graphene-MoS_2 interfaces

The interfaces formed between two dissimilar materials can be a little different from those of homojunctions because of the difference in the size and type of unit cells of the two materials on either side of the interface. Although graphene and transition metal dichalcogenides like MoS_2 have same type of unit cell (hexagonal) but the size of the unit cell is different. So, before discussing about electron transport across such heterojunctions, we redefine the nomenclature of the interfaces formed between graphene and MoS_2. When graphene (left side of the boundary) and MoS_2 (right side of the boundary) grains are rotated by equal angle with respect to the interface i.e. $\theta_L = \theta_R$, such heterojunctions are referred to as Class-I interface in this work, whereas when $\theta_L \neq \theta_R$ such interfaces will be referred to as Class-II interface from now onwards in this work.

Fig. 5.5(a) shows the thermionic transmission of the electrons across graphene-MoS_2 Class-I interface for various misorientation angles and carrier density of $1 \times 10^{12} cm^{-2}$. Due to the difference in the work function and electron affinity in graphene and MoS_2, the bands bend and a potential barrier is formed at the interface as shown in the previous chapter (Fig. 4.2 and Fig. 4.3). We find that the barrier height is independent of the misorientation angle and, consequently, we see in Fig. 5.5(b) that the interface resistance in Class-I heterojunctions is also independent of mismatch angle. We also note a strong dependence of interface resistance on carrier density as was also seen in chapter 4 (Fig. 4.3). At very high carrier densities, the interface resistance becomes comparable to the ballistic

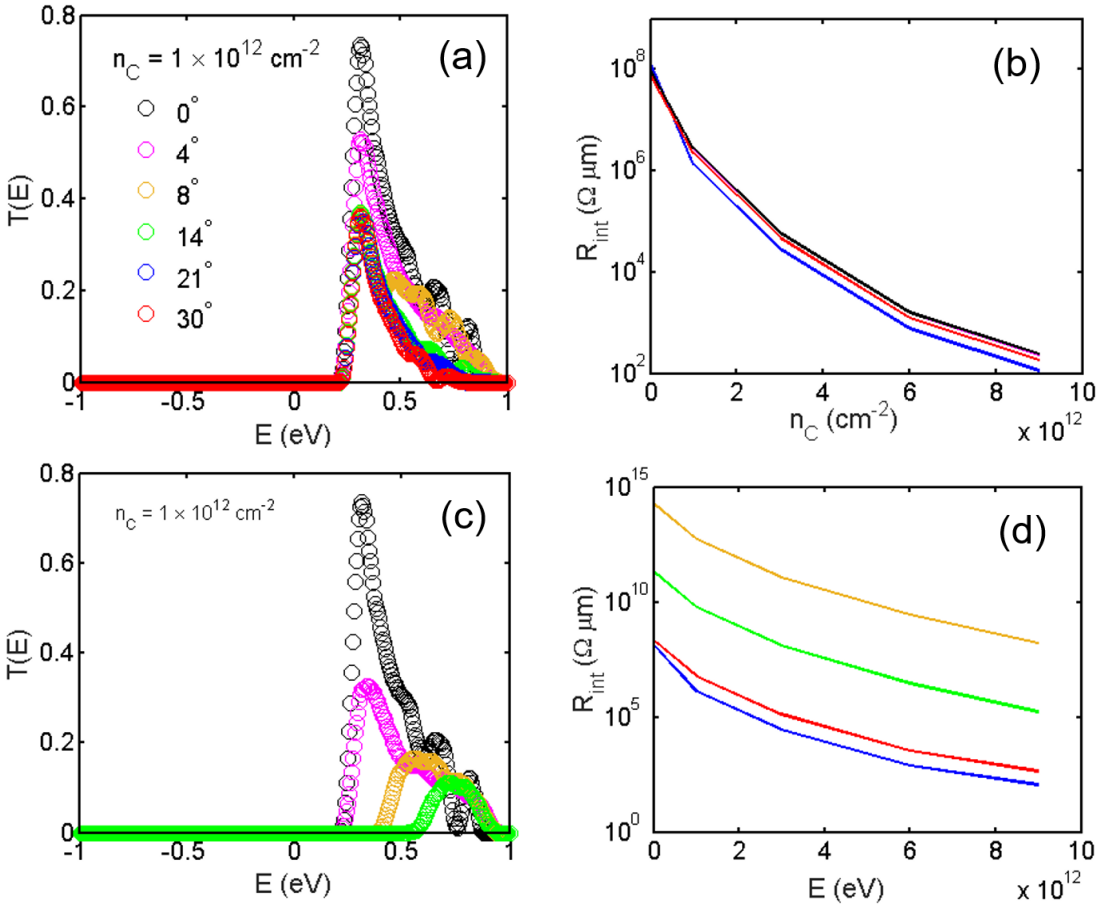

Figure 5.5. **(a)** shows transmission coefficient vs. energy for various misorientation angles across graphene-MoS_2 class-I interfaces. **(b)** shows the variation of interface resistance with carrier density for the same mismatch angles as plotted in **(a)**. Class-I graphene-MoS_2 interfaces show neglibible sensitivity towards misorientation angles. **(c)** shows transmission coefficient vs. energy for different misorientation angles in graphene-MoS_2 Class-II interfaces. On top of intrinsic barrier height, an additional transmission gap gets added up for such Class-II graphene-MoS_2 interfaces. The resulting interface resistance in Class-II interfaces vs. carrier density for different misorientation angles are plotted in **(d)**.

resistance of graphene and MoS_2 because at such high carrier densities the potential barrier almost disappears, which can also be seen in Fig. 5.6 and also in Fig. 5.8.

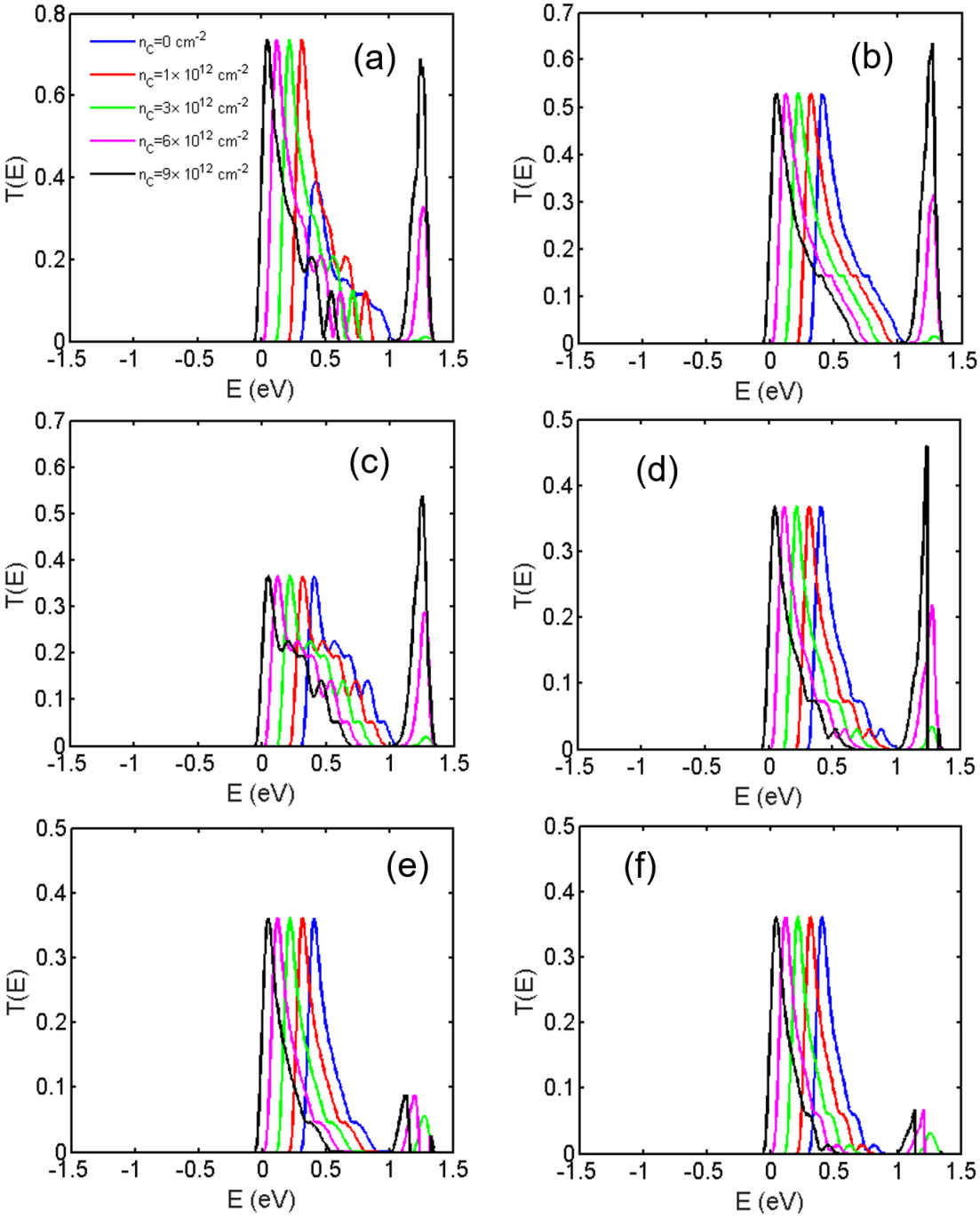

Figure 5.6. (a)-(f) show transmission coefficient vs. energy for various carrier densities in Class-I graphene-MoS_2 interfaces with misorientation angles of $0°$, $4°$, $8°$, $14°$, $21°$, and $30°$ respectively.

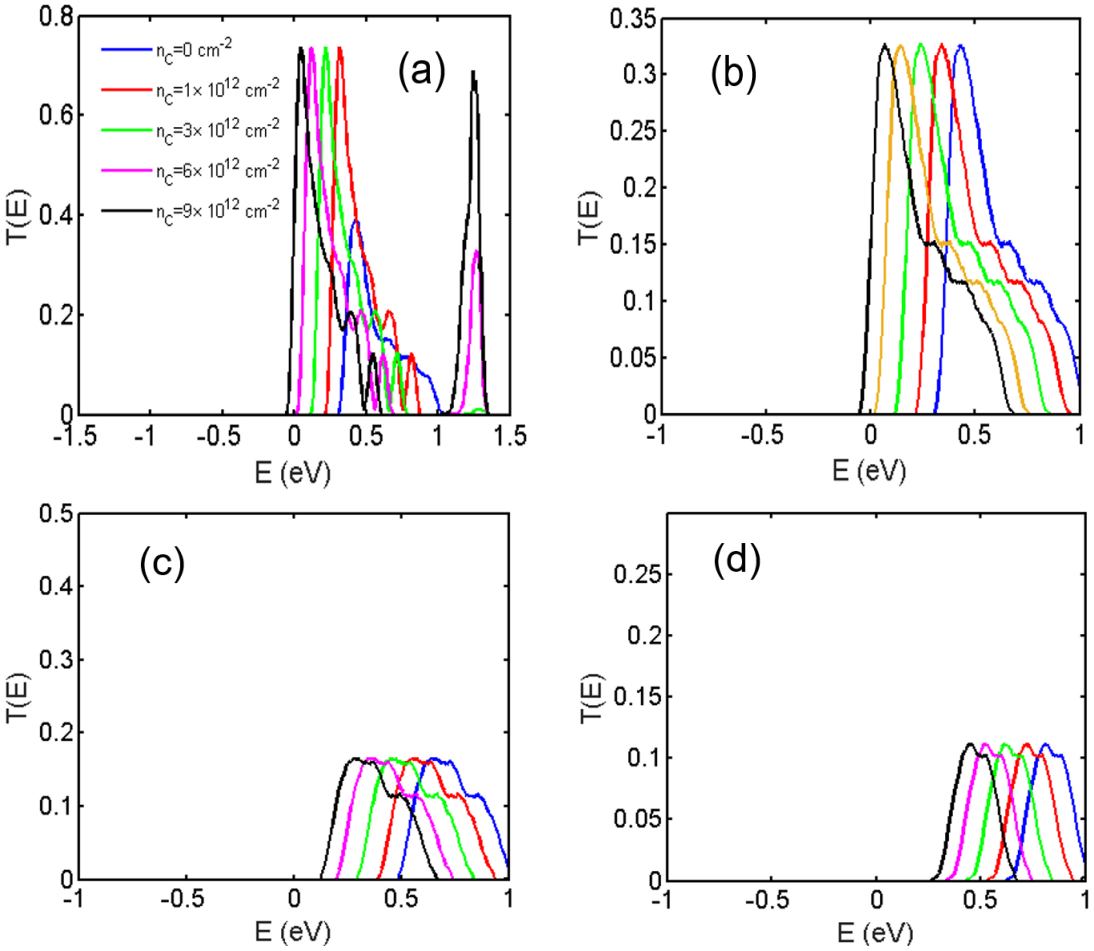

Figure 5.7. (a)-(d) show transmission coefficient vs. energy for various carrier densities in Class-II graphene-MoS_2 interfaces with misorientation angles of $0°$, $4°$, $8°$, and $14°$ respectively.

Fig. 5.5(c) shows transmission coefficient vs. energy for various misorientation angles in Class-II graphene-MoS_2 interface at a carrier density of $1\times10^{12}\ cm^{-2}$. It can also be seen that transmission coefficient decreases with increasing mismatch angle. A transmission gap gets added on top of existing potential barrier and the transmission gap widens with increasing misorientation angle. The transmission becomes zero for large mismatch angles (beyond $14°$). A strong dependence of interface resistance on misorientation angles in Class-II graphene-MoS_2 heterojunctions can be seen in Fig. 5.5(d).

In homojunctions like graphene-graphene and MoS_2-MoS_2 GBs, band alignment is independent of the position of the Fermi level, thus, transmission coefficient is independent of carrier densities in homojunctions. However, in heterojunctions, barrier height (band alignment) is a function of carrier density (position of the Fermi level) due to the difference in density of states of graphene and MoS_2. Transmission coefficient for different carrier densities in Class-I graphene-MoS_2 interface is plotted for $0°$, $4°$, $8°$, $14°$, $21°$, and $30°$ in Fig. 5.6 (a)-(f) respectively. It should be noted that at high carrier densities, the barrier height completely disappears in case of all mismatch angles. For Class-II graphene-MoS_2 junction, transmission coefficient for different carrier densities is plotted for $0°$, $4°$, $8°$, and $14°$ in Fig. 5.7 (a)-(d) respectively. For low mismatch angles, the potential barrier becomes zero at high carrier densities, but for large mismatch angles— $8°$, and $14°$— a barrier height exists even at high carrier densities as can be seen in Fig. 5.7(c) and (d), thereby, resulting into very large interface resistance.

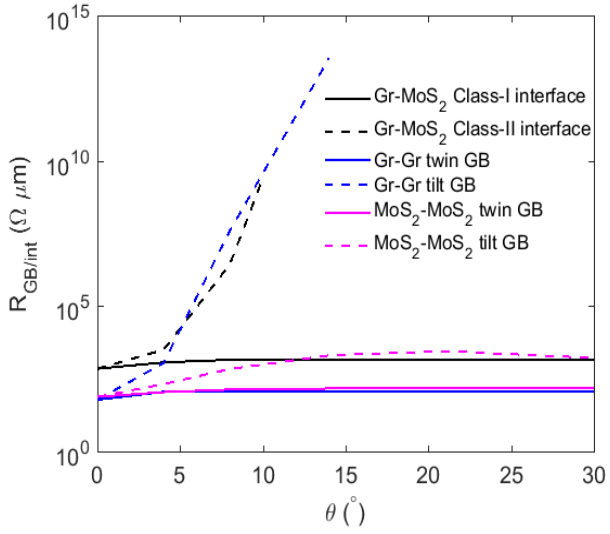

Figure 5.8. Comparison of GB/interface resistance vs. misorientation angles across Gr-Gr and MoS_2-MoS_2 GBs and Gr-MoS_2 interface.

Fig. 5.8 shows a comparison of the interface resistance among Gr-Gr, MoS_2-MoS_2, and Gr-MoS_2 interfaces. It can be seen that, in general, twin GBs in homojunctions and Class-I interfaces in heterojunctions show a very weak dependence on the degree of mismatch

between adjacent grains, whereas tilt GBs in homojunctions and Class-II interfaces in heterojunctions exhibit strong dependence on misorientation angles except in MoS_2, where both tilt and twin GBs are found to show a weak dependence on mismatch angles. The weak angle dependence in MoS_2-MoS_2 GBs can be attributed to the flat parabolic conduction band because of which the underlap in the bandstructures on the either side of the GB is quite small even at large mismatch angles.

5.4 Conclusion

In conclusion, we find that misorientation angle between two adjacent grains play a very significant role in both homojunctions and heterojunctions. We show that the grain boundary resistance across graphene GBs vary over a very wide range depending on the degree of mismatch between adjacent grains and type of GBs. Twin GBs are found to scatter electrons rather coherently, whereas tilt GBs strongly affect transmission of electrons across them. However in comparison with graphene, MoS_2 shows weaker dependence on misorientation angle for both twin and tilt GBs. This can be attributed to the flat parabolic bandstructure around K-valleys in MoS_2 as compared to the steep linear E-k relationship around K-valleys. We also show that the interface resistance across Class-II graphene-MoS_2 heterojunctions exhibit a strong dependence on misorientation angle, whereas the interface resistance in Class-I graphene-MoS_2 heterojunctions is almost independent of the effect of mismatch angles. However, Class-I interfaces exhibit a strong dependence on carrier densities.

CHAPTER 6

SUMMARY

We find that transport properties, both thermal and electronic, are significantly affected due to the presence of extrinsic factors such as finiteness of the 2D system, substrate, and mismatch angles between two grains at the interface. Our comprehensive study provides a deeper insight about the physics of how these external factors affect both heat and electron transport in van-Der Waals two-dimensional materials. In Chapter 2, we show that lattice thermal conductivity of intrinsic graphene keeps diverging with length due to quadratic nature of out-of-plane normal modes until these quadratic modes get partially linearized (renormalized) for large graphene samples; as a result the thermal conductivity gradually converges to a bulk value. The width dependence of thermal conductivity in graphene ribbons exhibit a Pouiselle hydrodynamic-like heat flow. GBs are found to reduce thermal conductivity considerably even in the presence of substrate. A bimodal phonon scattering mechanism is uncovered according to which small mismatch angles between adjacent grains can be captured by grain boundary roughness alone, whereas, for large mismatch angles a disordered patch is formed at the interface which significantly adds to the thermal boundary resistance. Interfaces are also found to affect the electronic transport between graphene-MoS_2 heterojunctions as well. Graphene-MoS_2 interfaces are found to be strongly dependent on applied gate voltage and at very high carrier densities, graphene-MoS_2 heterojunctions form Ohmic contacts. Interface resistance across such heterojunctions are found to be varying from 10^6 to 10^2 Ω μm, when the mismatch angle between graphene and MoS_2 is zero. However, we also show that interface resistance

across graphene-MoS_2 heterojunctions largely depend on misorientation angles between the grains and can vary over a very wide range— 10^2 to 10^{14} Ω μm.

The model we used to compute electronic interface resistance in homojunctions as well as heterojunctions neglect the possibility of tunneling across the interfaces, which can be included using WKB approximation in future work. The calculations of large samples with boundaries using first principles can be computationally expensive, however, can, possibly, be done in the future to check how the accuracy of this model.

BIBLIOGRAPHY

[1] Aksamija, Z., and Knezevic, I. Lattice thermal conductivity of graphene nanoribbons: Anisotropy and edge roughness scattering. *Appl. Phys. Lett. 98*, 14 (2011), 141919.

[2] Aksamija, Z., and Knezevic, I. Thermal transport in graphene nanoribbons supported on sio_2. *Phys. Rev. B 86* (2012), 165426.

[3] Allen, Philip B. Improved callaway model for lattice thermal conductivity. *Phys. Rev. B 88* (2013), 144302.

[4] Bae, Myung-Ho, Li, Zuanyi, Aksamija, Zlatan, Martin, Pierre N, Xiong, Feng, Ong, Zhun-Yong, Knezevic, Irena, and Pop, Eric. Ballistic to diffusive crossover of heat flow in graphene ribbons. *Nat Commun 4* (2013), 1734.

[5] Balandin, Alexander A. Thermal properties of graphene and nanostructured carbon materials. *Nat Mater 10* (2011).

[6] Balandin, Alexander A., Ghosh, Suchismita, Bao, Wenzhong, Calizo, Irene, Teweldebrhan, Desalegne, Miao, Feng, and Lau, Chun Ning. Superior thermal conductivity of single-layer graphene. *Nano Lett 8* (2008), 902–907.

[7] Barbarino, Giuliana, Melis, Claudio, and Colombo, Luciano. Intrinsic thermal conductivity in monolayer graphene is ultimately upper limited: A direct estimation by atomistic simulations. *Phys. Rev. B 91* (2015), 035416.

[8] Bardeen, John. Surface states and rectification at a metal semi-conductor contact. *Phys. Rev. 71* (1947), 717–727.

[9] Behranginia, Amirhossein, Yasaei, Poya, Majee, Arnab K., Long, Fei, Foss, Cameron James, Foroozan, Tara, Fuladi, Shadi, Hantehzadeh, Mohammadreza, Shahbazian-Yasar, Reza, Aksamija, Zlatan, and Salehi-Khojin, Amin. Direct-grown graphene and molybdenum disulfide lateral heterostructures for highly-packed all-two dimensional electronic circuitry. *Nat nano 12*, 3 (2016), 246–252.

[10] Berman, R., and Brock, J. C. F. The effect of isotopes on lattice heat conduction. i. lithium fluoride. *Proc. R. Soc. London, Ser. A 289* (1965), 46–65.

[11] Bonini, Nicola, Garg, Jivtesh, and Marzari, Nicola. Acoustic phonon lifetimes and thermal transport in free-standing and strained graphene. *Nano Lett 12* (2012), 2673–2678.

[12] Cahill, David G., Watson, S. K., and Pohl, R. O. Lower limit to the thermal conductivity of disordered crystals. *Phys. Rev. B 46* (1992), 6131–6140.

[13] Callaway, Joseph. Model for lattice thermal conductivity at low temperatures. *Phys. Rev. 113* (1959), 1046–1051.

[14] Cepellotti, Andrea, Fugallo, Giorgia, Paulatto, Lorenzo, Lazzeri, Michele, Mauri, Francesco, and Marzari, Nicola. Phonon hydrodynamics in two-dimensional materials. *Nat Commun 6*, 6400 (2015).

[15] Chang, C. W., Okawa, D., Garcia, H., Majumdar, A., and Zettl, A. Breakdown of fourier's law in nanotube thermal conductors. *Phys. Rev. Lett. 101* (2008), 075903.

[16] Chen, Gang. Nanoscale energy transport and conversion. heat and mass transfer.

[17] Chen, Jian-Hao, Jang, Chaun, Xiao, Shudong, Ishigami, Masa, and Fuhrer, Michael S. Intrinsic and extrinsic performance limits of graphene devices on sio2. *Nature Nano 3* (2008), 206 – 209.

[18] Chen, Shanshan, Moore, Arden L., Cai, Weiwei, Suk, Ji Won, An, Jinho, Mishra, Columbia, Amos, Charles, Magnuson, Carl W., Kang, Junyong, Shi, Li, and Ruoff, Rodney S. Raman measurements of thermal transport in suspended monolayer graphene of variable sizes in vacuum and gaseous environments. *ACS Nano 5* (2011), 321–328.

[19] Clark, Kendal W., Zhang, X.-G., Vlassiouk, Ivan V., He, Guowei, Feenstra, Randall M., and Li, An-Ping. Spatially resolved mapping of electrical conductivity across individual domain (grain) boundaries in graphene. *ACS Nano 7* (2013), 7956–7966.

[20] Cui, Xu, Lee, Gwan-Hyoung, Kim, Young Duck, Arefe, Ghidewon, Huang, Pinshane Y., Lee, Chul-Ho, Chenet, Daniel A., Zhang, Xian, Wang, Lei, Ye, Fan, Pizzocchero, Filippo, Jessen, Bjarke S., Watanabe, Kenji, Taniguchi, Takashi, Muller, David A., Low, Tony, Kim, Philip, and Hone, James. Multi-terminal transport measurements of mos2 using a van der waals heterostructure device platform. *Nat Nano 10*, 6 (2015), 534–540.

[21] Das, Saptarshi, Chen, Hong-Yan, Penumatcha, Ashish Verma, and Appenzeller, Joerg. High performance multilayer mos2 transistors with scandium contacts. *Nano Lett 13* (2013), 100–105.

[22] Dhar, Abhishek. Heat transport in low-dimensional systems. *Advances in Physics 57* (2008), 457–537.

[23] Dorgan, Vincent E., Bae, Myung-Ho, and Pop, Eric. Mobility and saturation velocity in graphene on sio2. *Appl. Phys. Lett. 97*, 8 (2010).

[24] Fong, Kin Chung, and Schwab, K. C. Ultrasensitive and wide-bandwidth thermal measurements of graphene at low temperatures. *Phys. Rev. X 2* (2012), 031006.

[25] Ghosh, S., Calizo, I., Teweldebrhan, D., Pokatilov, E. P., Nika, D. L., Balandin, A. A., Bao, W., Miao, F., and Lau, C. N. Extremely high thermal conductivity of graphene: Prospects for thermal management applications in nanoelectronic circuits. *Appl. Phys. Lett. 92*, 15 (2008), 151911.

[26] Giannozzi, Paolo, Baroni, Stefano, Bonini, Nicola, Calandra, Matteo, Car, Roberto, Cavazzoni, Carlo, Ceresoli, Davide, Chiarotti, Guido L, Cococcioni, Matteo, Dabo, Ismaila, Corso, Andrea Dal, de Gironcoli, Stefano, Fabris, Stefano, Fratesi, Guido, Gebauer, Ralph, Gerstmann, Uwe, Gougoussis, Christos, Kokalj, Anton, Lazzeri, Michele, Martin-Samos, Layla, Marzari, Nicola, Mauri, Francesco, Mazzarello, Riccardo, Paolini, Stefano, Pasquarello, Alfredo, Paulatto, Lorenzo, Sbraccia, Carlo, Scandolo, Sandro, Sclauzero, Gabriele, Seitsonen, Ari P, Smogunov, Alexander, Umari, Paolo, and Wentzcovitch, Renata M. Quantum espresso: a modular and open-source software project for quantum simulations of materials. *J. Phys.: Condens. Matter 21*, 39 (2009), 395502.

[27] Gilat, G., and Raubenheimer, L. J. Accurate numerical method for calculating frequency-distribution functions in solids. *Phys. Rev. 144* (1966), 390–395.

[28] Gurvitch, M. Ioffe-regel criterion and resistivity of metals. *Phys. Rev. B 24* (1981), 7404–7407.

[29] Huang, Pinshane Y., Ruiz-Vargas, Carlos S., van der Zande, Arend M., Whitney, William S., Levendorf, Mark P., Kevek, Joshua W., Garg, Shivank, Alden, Jonathan S., Hustedt, Caleb J., Zhu, Ye, Park, Jiwoong, McEuen, Paul L., and Muller, David A. Grains and grain boundaries in single-layer graphene atomic patchwork quilts. *Nature 469*, 7330 (2011), 389–392.

[30] Huang, Zhen, Fisher, Timothy S., and Murthy, Jayathi Y. Simulation of phonon transmission through graphene and graphene nanoribbons with a greens function method. *J. Appl. Phys. 108*, 9 (2010), 094319.

[31] Jeong, Changwook, Datta, Supriyo, and Lundstrom, Mark. Full dispersion versus debye model evaluation of lattice thermal conductivity with a landauer approach. *J. Appl. Phys. 109*, 7 (2011), 073718.

[32] Kaasbjerg, Kristen, Thygesen, Kristian S., and Jacobsen, Karsten W. Phonon-limited mobility in n-type single-layer mos_2 from first principles. *Phys. Rev. B 85* (2012), 115317.

[33] Klemens, P.G. Theory of thermal conduction in thin ceramic films. *Int. J. Thermophys. 22* (2001), 265–275.

[34] Klemens, P.G., and Pedraza, D.F. Thermal conductivity of graphite in the basal plane. *Carbon 32* (1994), 735 – 741.

[35] Koepke, Justin C., Wood, Joshua D., Estrada, David, Ong, Zhun-Yong, He, Kevin T., Pop, Eric, and Lyding, Joseph W. Atomic-scale evidence for potential barriers and strong carrier scattering at graphene grain boundaries: A scanning tunneling microscopy study. *ACS Nano 7* (2013), 75–86.

[36] Kong, B. D., Paul, S., Nardelli, M. Buongiorno, and Kim, K. W. First-principles analysis of lattice thermal conductivity in monolayer and bilayer graphene. *Phys. Rev. B 80* (2009), 033406.

[37] Lee, Jae-Ung, Yoon, Duhee, Kim, Hakseong, Lee, Sang Wook, and Cheong, Hyeonsik. Thermal conductivity of suspended pristine graphene measured by raman spectroscopy. *Phys. Rev. B 83* (2011), 081419.

[38] Lee, Sangyeop, Broido, David, Esfarjani, Keivan, and Chen, Gang. Hydrodynamic phonon transport in suspended graphene. *Nat Commun 6* (2015), 6290.

[39] Li, Baowen, and Wang, Jiao. Anomalous heat conduction and anomalous diffusion in one-dimensional systems. *Phys. Rev. Lett. 91* (2003), 044301.

[40] Lindsay, L., Broido, D. A., and Mingo, Natalio. Flexural phonons and thermal transport in graphene. *Phys. Rev. B 82* (2010), 115427.

[41] Lindsay, L., Li, Wu, Carrete, Jesús, Mingo, Natalio, Broido, D. A., and Reinecke, T. L. Phonon thermal transport in strained and unstrained graphene from first principles. *Phys. Rev. B 89* (2014), 155426.

[42] Liu, Yuan, Wu, Hao, Cheng, Hung-Chieh, Yang, Sen, Zhu, Enbo, He, Qiyuan, Ding, Mengning, Li, Dehui, Guo, Jian, Weiss, Nathan O., Huang, Yu, and Duan, Xiangfeng. Toward barrier free contact to molybdenum disulfide using graphene electrodes. *Nano Lett 15* (2015), 3030–3034.

[43] Ly, Thuc Hue, Perello, David J., Zhao, Jiong, Deng, Qingming, Kim, Hyun, Han, Gang Hee, Chae, Sang Hoon, Jeong, Hye Yun, and Lee, Young Hee. Misorientation-angle-dependent electrical transport across molybdenum disulfide grain boundaries. *Nat Commun 7* (2016), 10426.

[44] Ma, Jinlong, Li, Wu, and Luo, Xiaobing. Examining the callaway model for lattice thermal conductivity. *Phys. Rev. B 90* (2014), 035203.

[45] Ma, Nan, and Jena, Debdeep. Charge scattering and mobility in atomically thin semiconductors. *Phys. Rev. X 4* (2014), 011043.

[46] Mariani, Eros, and von Oppen, Felix. Flexural phonons in free-standing graphene. *Phys. Rev. Lett. 100* (2008), 076801.

[47] Mark Lundstrom, Changwook Jeong. *Near-equilibrium transport- Fundamentals and applications*, vol. 2. World Scientific, 2013.

[48] Mei, S., Maurer, L. N., Aksamija, Z., and Knezevic, I. Full-dispersion monte carlo simulation of phonon transport in micron-sized graphene nanoribbons. *J. Appl. Phys. 116*, 16 (2014), 164307.

[49] Morelli, D. T., Heremans, J. P., and Slack, G. A. Estimation of the isotope effect on the lattice thermal conductivity of group iv and group iii-v semiconductors. *Phys. Rev. B 66* (2002), 195304.

[50] Muoz, Enrique, Lu, Jianxin, and Yakobson, Boris I. Ballistic thermal conductance of graphene ribbons. *Nano Lett 10* (2010), 1652–1656.

[51] Narayan, Onuttom, and Ramaswamy, Sriram. Anomalous heat conduction in one-dimensional momentum-conserving systems. *Phys. Rev. Lett. 89* (2002), 200601.

[52] Nika, D. L., Ghosh, S., Pokatilov, E. P., and Balandin, A. A. Lattice thermal conductivity of graphene flakes: Comparison with bulk graphite. *Appl. Phys. Lett. 94*, 20 (2009), 203103.

[53] Nika, D. L., Pokatilov, E. P., Askerov, A. S., and Balandin, A. A. Phonon thermal conduction in graphene: Role of umklapp and edge roughness scattering. *Phys. Rev. B 79* (Apr 2009), 155413.

[54] Novikov, N.V., Podoba, A.P., Shmegera, S.V., Witek, A., Zaitsev, A.M., Denisenko, A.B., Fahrner, W.R., and Werner, M. Influence of isotopic content on diamond thermal conductivity. *Diamond Relat. Mater. 8* (1999), 1602 – 1606.

[55] Ong, Zhun-Yong, and Pop, Eric. Effect of substrate modes on thermal transport in supported graphene. *Phys. Rev. B 84* (2011), 075471.

[56] Park, Minkyu, Lee, Sun-Chul, and Kim, Yong-Sung. Length-dependent lattice thermal conductivity of graphene and its macroscopic limit. *J. Appl. Phys. 114* (2013), 053506.

[57] Prasher, Ravi. Thermal boundary resistance and thermal conductivity of multiwalled carbon nanotubes. *Phys. Rev. B 77* (2008), 075424.

[58] Prosen, Toma ž, and Campbell, David K. Momentum conservation implies anomalous energy transport in 1d classical lattices. *Phys. Rev. Lett. 84* (2000), 2857–2860.

[59] Qiu, Bo, and Ruan, Xiulin. Reduction of spectral phonon relaxation times from suspended to supported graphene. *Appl. Phys. Lett. 100*, 19 (2012), 193101.

[60] R. Saito, M.S. Dresselhaus, G. Dresselhaus. *Physical properties of carbon nanotubes*. Imperial College Press: London, 1998.

[61] Seol, Jae Hun, Jo, Insun, Moore, Arden L., Lindsay, Lucas, Aitken, Zachary H., Pettes, Michael T., Li, Xuesong, Yao, Zhen, Huang, Rui, Broido, David, Mingo, Natalio, Ruoff, Rodney S., and Shi, Li. Two-dimensional phonon transport in supported graphene. *Science 328*, 5975 (2010), 213–216.

[62] Serov, Andrey Y., Ong, Zhun-Yong, and Pop, Eric. Effect of grain boundaries on thermal transport in graphene. *Appl. Phys. Lett. 102*, 3 (2013).

[63] Tuan, Dinh Van, Kotakoski, Jani, Louvet, Thibaud, Ortmann, Frank, Meyer, Jannik C., and Roche, Stephan. Scaling properties of charge transport in polycrystalline graphene. *Nano Lett 13* (2013), 1730–1735.

[64] Wei, Zhiyong, Yang, Juekuan, Bi, Kedong, and Chen, Yunfei. Mode dependent lattice thermal conductivity of single layer graphene. *J. Appl. Phys. 116*, 15 (2014), 153503.

[65] Xu, Xiangfan, Pereira, Luiz F. C., Wang, Yu, Wu, Jing, Zhang, Kaiwen, Zhao, Xiangming, Bae, Sukang, Bui, Cong Tinh, Xie, Rongguo, and Thong, John T. L. Length-dependent thermal conductivity in suspended single-layer graphene. *Nat Commun 5* (2014), 3689.

[66] Yang, Nuo, Ni, Xiaoxi, Jiang, Jin-Wu, and Li, Baowen. How does folding modulate thermal conductivity of graphene? *Appl. Phys. Lett. 100* (2012), 093107.

[67] Yasaei, Poya, Fathizadeh, Arman, Hantehzadeh, Reza, Majee, Arnab K., El-Ghandour, Ahmed, Estrada, David, Foster, Craig, Aksamija, Zlatan, Khalili-Araghi, Fatemeh, and Salehi-Khojin, Amin. Bimodal phonon scattering in graphene grain boundaries. *Nano Lett. 15* (2015), 4532–4540.

[68] Yazyev, Oleg V., and Louie, Steven G. Electronic transport in polycrystalline graphene. *Nat Mater 9* (2010), 806–809.

[69] Yoon, Jongwon, Park, Woojin, Bae, Ga-Yeong, Kim, Yonghun, Jang, Hun Soo, Hyun, Yujun, Lim, Sung Kwan, Kahng, Yung Ho, Hong, Woong-Ki, Lee, Byoung Hun, and Ko, Heung Cho. Highly flexible and transparent multilayer mos2 transistors with graphene electrodes. *Small 9*, 19 (2013), 3295–3300.

[70] Yu, Lili, Lee, Yi-Hsien, Ling, Xi, Santos, Elton J. G., Shin, Yong Cheol, Lin, Yuxuan, Dubey, Madan, Kaxiras, Efthimios, Kong, Jing, Wang, Han, and Palacios, Toms. Graphene/mos2 hybrid technology for large-scale two-dimensional electronics. *Nano Lett 14* (2014), 3055–3063.

[71] Yu, Woo Jong, Li, Zheng, Zhou, Hailong, Chen, Yu, Wang, Yang, Huang, Yu, and Duan, Xiangfeng. Vertically stacked multi-heterostructures of layered materials for logic transistors and complementary inverters. *Nat Mater 12*, 3 (2013), 246–252.

[72] Yu, Zhihao, Ong, Zhun-Yong, Pan, Yiming, Cui, Yang, Xin, Run, Shi, Yi, Wang, Baigeng, Wu, Yun, Chen, Tangsheng, Zhang, Yong-Wei, Zhang, Gang, and Wang, Xinran. Realization of room-temperature phonon-limited carrier transport in monolayer mos2 by dielectric and carrier screening. *Adv Mater 28* (2016), 547–552.

[73] Yu, Zhihao, Pan, Yiming, Shen, Yuting, Wang, Zilu, Ong, Zhun-Yong, Xu, Tao, Xin, Run, Pan, Lijia, Wang, Baigeng, Sun, Litao, Wang, Jinlan, Zhang, Gang, Zhang, Yong Wei, Shi, Yi, and Wang, Xinran. Towards intrinsic charge transport in monolayer molybdenum disulfide by defect and interface engineering. *Nat Commun 5* (2014), 5290.